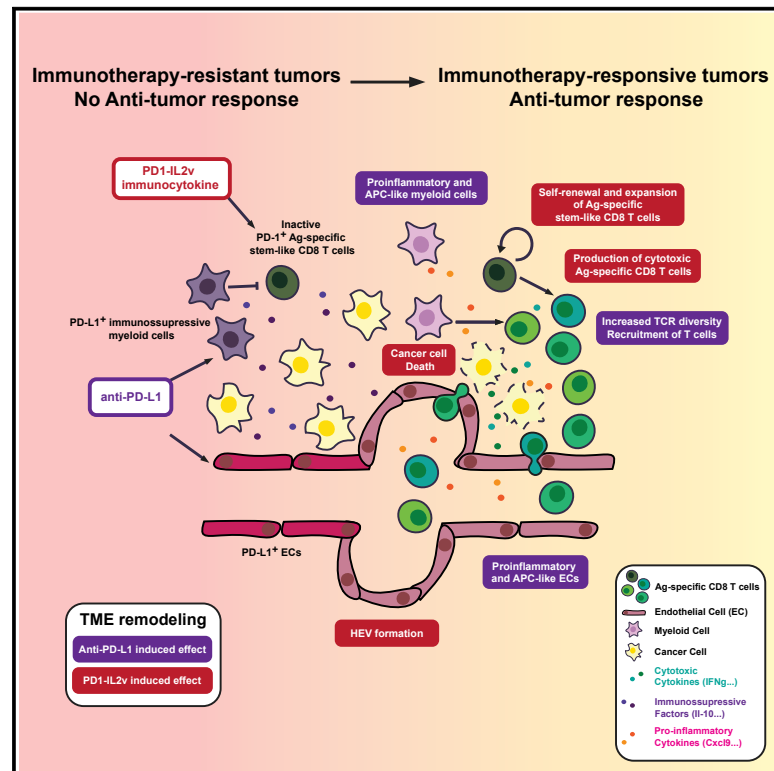


Immunity

Bispecific PD1-IL2v and anti-PD-L1 break tumor immunity resistance by enhancing stem-like tumor-reactive CD8⁺ T cells and reprogramming macrophages

Graphical abstract



Authors

Mélanie Tichet, Stephan Wullschleger, Agnieszka Chryplewicz, ..., Pablo Umaña, Christian Klein, Douglas Hanahan

Correspondence

stephanw987@gmail.com (S.W.), douglas.hanahan@epfl.ch (D.H.)

In brief

Most cancer patients respond transiently to immunotherapy, highlighting the importance of understanding the mechanisms underlying resistance. Tichet et al. reveal that the immunocytokine PD1-IL2v combined with anti-PD-L1 synergize to enable anti-tumor immunity against immunotherapy-resistant tumors. PD1-IL2v promotes stem-like, tumor-reactive CD8⁺ T cell expansion and high endothelial venule formation, whereas anti-PD-L1 reprograms macrophages and tumor vasculature to antigen-presenting and pro-inflammatory phenotypes.

Highlights

- PD1-IL2v promotes and expands pre-existing stem-like and tumor-reactive CD8⁺ T cells
- PD1-IL2v treatment leads to tumor regression that can be sustained by anti-PD-L1
- Anti-PD-L1 reprograms immunosuppressive TAMs and tumor vasculature to be pro-inflammatory
- Anti-PD-L1 synergizes with PD1-IL2v to improve the efficacy of tumor immunotherapy



Article

Bispecific PD1-IL2v and anti-PD-L1 break tumor immunity resistance by enhancing stem-like tumor-reactive CD8⁺ T cells and reprogramming macrophages

Mélanie Tichet,^{1,2,3,4,10} Stephan Wullschleger,^{1,2,9,10,*} Agnieszka Chryplewicz,^{1,2,4} Nadine Fournier,⁵ Rachel Marcone,⁵ Annamaria Kauzlaric,⁵ Krisztian Homicsko,^{1,2,4,6,7} Laura Codarri Deak,⁸ Pablo Umaña,⁸ Christian Klein,⁸ and Douglas Hanahan^{1,2,3,4,11,*}

¹Swiss Institute for Experimental Cancer Research (ISREC), EPFL, Lausanne, Switzerland

²Swiss Cancer Center Leman (SCCL), Lausanne, Switzerland

³Ludwig Institute for Cancer Research, Lausanne Branch, 1011 Lausanne, Switzerland

⁴Agora Translational Cancer Research Center, Rue du Bugnon 25A, 1011 Lausanne, Switzerland

⁵Bioinformatics Core Facility, SIB Swiss Institute of Bioinformatics, Lausanne, Switzerland

⁶Department of Oncology, CHUV, 46 Rue Bugnon, 1011 Lausanne, Switzerland

⁷Center for Personalized Oncology, CHUV, 46 Rue Bugnon, 1011 Lausanne, Switzerland

⁸Roche-Innovation Center Zurich, 8952 Schlieren, Switzerland

⁹Present address: Molecular Partners AG, 8952 Schlieren, Switzerland

¹⁰These authors contributed equally

¹¹Lead contact

*Correspondence: stephanw987@gmail.com (S.W.), douglas.hanahan@epfl.ch (D.H.)

<https://doi.org/10.1016/j.immuni.2022.12.006>

SUMMARY

Immunotherapies have shown remarkable, albeit tumor-selective, therapeutic benefits in the clinic. Most patients respond transiently at best, highlighting the importance of understanding mechanisms underlying resistance. Herein, we evaluated the effects of the engineered immunocytokine PD1-IL2v in a mouse model of *de novo* pancreatic neuroendocrine cancer that is resistant to checkpoint and other immunotherapies. PD1-IL2v utilizes anti-PD-1 as a targeting moiety fused to an immuno-stimulatory IL-2 cytokine variant (IL2v) to precisely deliver IL2v to PD-1⁺ T cells in the tumor microenvironment. PD1-IL2v elicited substantial infiltration by stem-like CD8⁺ T cells, resulting in tumor regression and enhanced survival in mice. Combining anti-PD-L1 with PD1-IL2v sustained the response phase, improving therapeutic efficacy both by reprogramming immunosuppressive tumor-associated macrophages and enhancing T cell receptor (TCR) immune repertoire diversity. These data provide a rationale for clinical trials to evaluate the combination therapy of PD1-IL2v and anti-PD-L1, particularly in immunotherapy-resistant tumors infiltrated with PD-1⁺ stem-like T cells.

INTRODUCTION

The development of cancer immunotherapies has revolutionized the treatment of cancer patients. At the forefront of clinically approved immunotherapies are immune checkpoint inhibitors.^{1–3} Despite extraordinary remissions, the majority of cancer patients either do not respond to immune checkpoint blockade (ICB) or will acquire resistance to this treatment modality.⁴ Hence, there is need for immunomodulatory strategies that disrupt operative mechanisms underlying non-responsiveness.

One approach involves stimulating effector T cells by cytokines such as interleukin-2 (IL-2), which has been approved for the treatment of metastatic melanoma and renal cell carcinoma.⁵ IL-2 acts by binding to the IL-2 receptor predominantly expressed on T lymphocytes.⁶ However, IL-2 also stimulates the differentiation, suppressive function, and homeostasis of regula-

tory T cells (Tregs) that counterbalance effector T cell activity.⁷ Moreover, therapeutic application of IL-2 is compromised by its short half-life, necessitating high dosing with considerable toxicity.⁵ To overcome the limitations of IL-2 as a therapeutic agent, two strategies have evolved: tumor-targeted rather than systemic delivery^{8,9} and engineered variants of IL-2 that preferentially activate IL-2-mediated signaling through the IL-2Rβγ heterodimeric receptor without concomitantly activating IL-2Rα (CD25) and consequentially amplifying Tregs.^{10–15} Both strategies have been incorporated into PD1-IL2v, a bispecific antibody molecule (dubbed an immunocytokine) that combines CD8⁺ T cell targeting via PD-1 binding with an IL-2 variant (IL2v) defective in binding to CD25.¹⁶

Several recent studies have described the importance of CD8⁺ T cell stemness in chronic viral infection and cancer.^{2,16–20} These antigen-experienced stem-like CD8⁺ T cells express both the



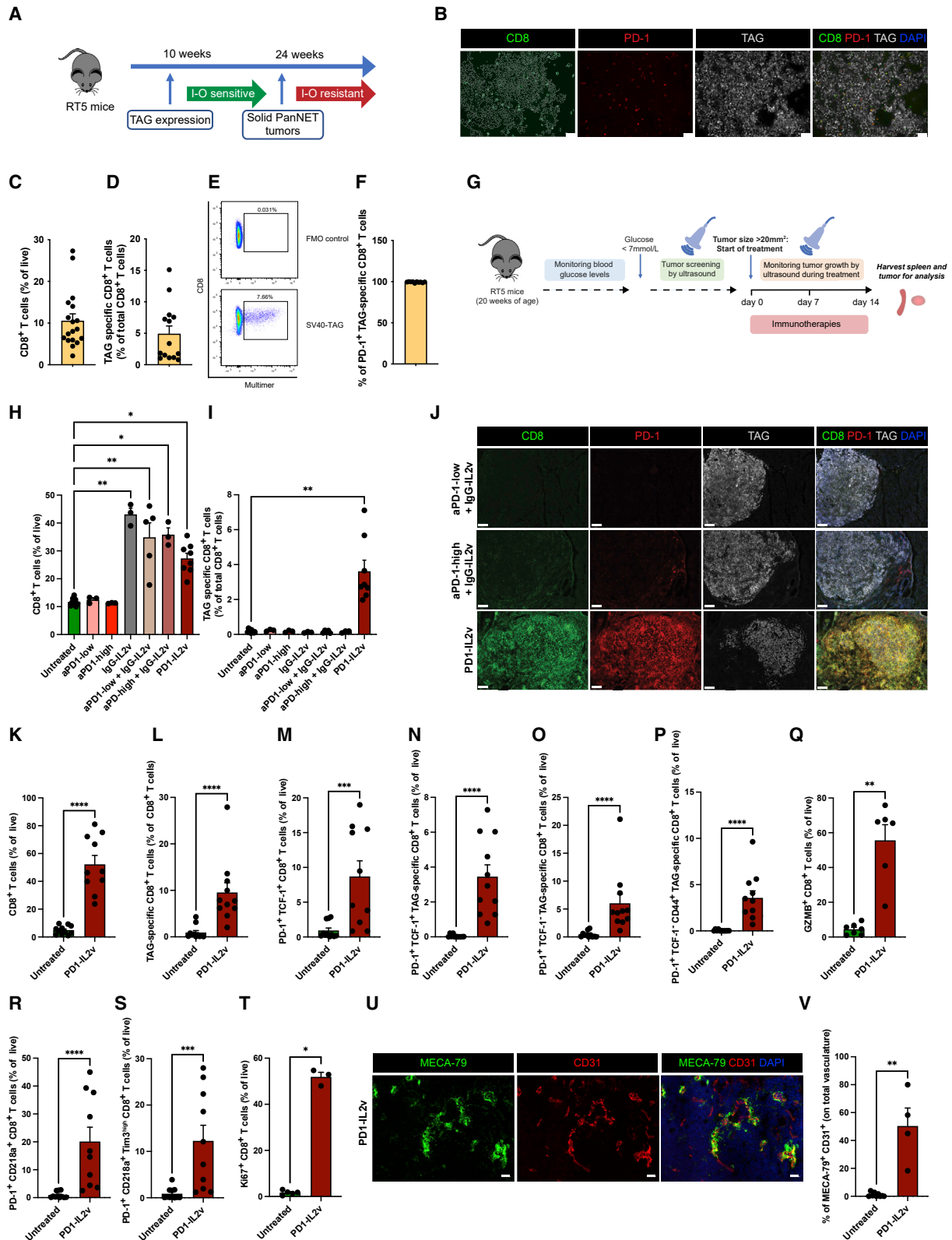


Figure 1. PanNETs that develop in RT5 mice are infiltrated with CD8⁺ T cells, and PD1-IL2v treatment leads to the expansion of TAG-specific CD8⁺ T cells in spleen and tumors

(A) Schematic of tumor development in RT5 mice, indicating sensitivity to immune-oncology (I-O) treatments of premalignant lesions and resistance to I-O of fully formed PanNETs.

(legend continued on next page)

high mobility group-box (HMG-box) transcription factor TCF-1 and the checkpoint receptor PD-1 and possess self-renewal capacity in response to viral or tumor antigens. The PD-1⁺TCF-1⁺ CD8⁺ T cells act as a reservoir that can continually produce TCF-1⁻ effector T cells exhibiting cytotoxic functions. Notably, the aforementioned PD1-IL2v has been recently shown to enhance the abundance and activity of PD-1⁺ stem-like CD8⁺ T cells.¹⁶ Despite heightened awareness of the role of PD-1⁺ TCF-1⁺ CD8⁺ T cells in physiological immune responses and the demonstrable capability of PD1-IL2v to expand them, their involvement in anti-tumor immunity and their potential roles in overcoming intrinsic and adaptive resistance to T cell immunotherapy have not been thoroughly explored. Herein, we evaluate this immunocytokine in a genetically engineered model of pancreatic neuroendocrine tumors (PanNETs) in which tumors express an immunostimulatory neoantigen and yet are resistant to spontaneous and therapeutic tumor immunity. Our results reveal remarkable complementarity from combining PD1-IL2v with anti-PD-L1, collectively promoting and expanding pre-existing stem-like and tumor-reactive CD8⁺ T cells and remodeling immunosuppressive tumor-associated macrophages and vasculature, respectively, thereby eliciting efficacious anti-tumor immunity.

RESULTS

The RT5 model is a prototype for studying immunotherapies

In the RIP1-Tag5 (RT5) transgenic mouse model, expression of the driving oncogene encoding the SV40 large T-antigen (TAG) oncoprotein begins at ten weeks of age in the insulin-producing pancreatic islet beta cells (Figure 1A).^{21–24} Consequently, RT5 mice develop a spontaneous immune response against TAG, resulting in lymphocyte infiltration in premalignant lesions. During tumorigenesis, spontaneous tumors developing in RT5 mice establish a barrier to immune destruction involving, for example, modulation of the tumor vasculature.^{23,24} While mice displaying premalignant lesions are responsive to a vaccine against TAG,²⁵ established solid tumors that form at around six months of age display resistance both to vaccines against TAG and to immune checkpoint inhibitors^{25,26} (Figure 1A). Extending upon previous

analyses, we assessed the number and phenotype of tumor-infiltrating CD8⁺ T cells in solid tumors of RT5 mice. The islet tumors were modestly infiltrated with CD8⁺ T cells, which expressed the immune checkpoint receptor PD-1 (Figure 1B). Flow cytometric analyses revealed that CD8⁺ T cell infiltration comprised ~ 10% of total cells (Figure 1C). Of these, ~ 5% of intratumoral CD8⁺ T cells were specific to the TAG peptide VVYDFLKC, as defined by multimer staining (Figures 1D and 1E), and more than 90% of these TAG-specific CD8⁺ T cells were positive for PD-1 (Figures 1B and 1F).

The PD1-IL2v immunocytokine shows superior efficacy compared to individual anti-PD-1 and IL2v treatments

Seeking to disrupt the demonstrable intrinsic resistance to immunotherapy in this model, we evaluated the effects of the PD1-IL2v immunocytokine compared with its bioactive components, anti-PD-1 and IL2v. Given that more than 90% of TAG tumor-antigen-specific CD8⁺ T cells are PD-1⁺ in islet tumors, we reasoned that IL2v linked to PD-1 in the PD1-IL2v immunocytokine could be delivered into tumors to stimulate the local expansion of CD8⁺ T cells. To explore this hypothesis, we conducted pharmacodynamic studies in tumor-bearing RT5 mice. A hallmark of islet tumors is the secretion of insulin resulting in hypoglycemia, and monitoring the blood glucose concentration serves as a surrogate biomarker for the presence of islet tumors. Upon observing a drop in blood glucose concentration below 7 mmol/L, mice were screened for the presence of tumors by ultrasound imaging (Figure 1G). RT5 mice were selected for treatment based on the tumor size, and tumor progression was longitudinally monitored by ultrasound imaging (Figure 1G). We first assessed the immune response in the spleen following two weeks of treatment. Notably, the dosing of PD1-IL2v is by design lower than that required to block all the PD-1 molecules on T cells, and rather is optimized to deliver an efficacious but not toxic dose of IL2v to T cells in the tumor microenvironment (TME) and lymphoid organs.¹⁶ To evaluate the advantage of PD1-IL2v vs. separately supplied anti-PD-1 and a non-targeted IgG-IL2v immunocytokine, the latter were tested individually and in combination and compared to PD1-IL2v. For anti-PD-1, two concentrations were used: anti-PD-1^{low}, representing equimolar amounts to PD-1 in the bifunctional molecule, and

(B) IF staining for CD8, PD-1, and TAG of tumors from RT5 mice (scale bar, 50µm; n = 14).

(C–D) Flow cytometry analyses of intratumoral CD8⁺ T cells (C), TAG-specific CD8⁺ T cells (D)(n = 14–18).

(E) Flow cytometry plot, showing no multimer control (FMO) and staining with a multimer against TAG-specific CD8⁺ T cells.

(F) Flow cytometry analyses of intratumoral PD-1⁺ TAG-specific CD8⁺ T cells (n = 14).

(G) Schematic depicting monitoring of mice based on blood glucose concentration as a surrogate biomarker for islet tumors and selection of RT5 mice for *in vivo* efficacy treatment based on tumor burden measured by ultrasound imaging. For pharmacodynamic studies, tumor-bearing RT5 mice were treated for 14 days.

(H and I) Flow cytometry analyses of splenic CD8⁺ T cells (H), and TAG tumor antigen-specific CD8⁺ T cells (I) (n = 3–10).

(J) IF images of tumors of the different treatment groups stained for CD8, PD-1, and TAG (scale bar, 200µm; n = 4–6).

(K–T) Flow cytometry analyses of intratumoral CD8⁺ T cells (K), TAG-specific CD8⁺ T cells (L), stem-like resource PD-1⁺TCF1⁺ CD8⁺ T cells (M), stem-like resource PD-1⁺TCF-1⁺ TAG-specific CD8⁺ T cells (N), stem-like progeny PD-1⁺TCF1⁺ TAG-specific CD8⁺ T cells (O), effector PD-1⁺TCF-1⁻ CD44⁺ TAG-specific CD8⁺ T cells (P), cytotoxic Granzyme B⁺ (GZMB) CD8⁺ T cells (Q), fresh effector PD-1⁺CD218a⁺ CD8⁺ T cells (R), better effector PD-1⁺CD218⁺Tim3^{high} CD8⁺ T cells (S), and Ki67⁺ CD8⁺ T cells (T) (n = 3–10).

(U) IF images of tumors for MECA79⁺CD31⁺ HEVs (scale bar, 20µm).

(V) HEV quantification in the entire area of a tumor tissue section. Untreated (n = 10), PD1-IL2v (n = 4).

Data in all quantitative panels are presented as mean ± SEM.

Experiments were independently repeated at least twice.

Statistical analysis: one-way ANOVA Kruskal-Wallis with Dunn's multiple comparisons test (compared to the untreated group), Figures 1H and 1I = *p < 0.05, **p < 0.01, Mann-Whitney test, Figure 1K–V = *p < 0.05, **p < 0.01, ***p < 0.001, ****p < 0.0001.

Please also see Figures S1A–S1E.

anti-PD-1^{-high}, replicating the dose employed for the monoclonal anti-PD-1 antibody in the therapeutic setting of ICB. Upon two weeks of treatment, we observed a 3- to 4-fold expansion of total CD8⁺ T cells in the spleens for all treatment groups where IL2v was co-administered, including PD1-IL2v (Figure 1H). However, flow cytometry-based analyses of spleens from treated mice revealed that TAG-specific CD8⁺ T cells were exclusively expanded to ~4% of total CD8⁺ T cells in the PD-IL2v treatment group (Figure 1I). The percentage of CD4⁺ T cells was decreased in the IgG-IL2v-treated but not in the PD1-IL2v-treated cohort (Figure S1A). Notably, as previously reported,¹² treatment with IL2v-containing molecules did not result in an expansion of Tregs (Figure S1B).

These data were corroborated by immunofluorescent staining of tumor tissue sections. PD1-IL2v treatment elicited an intensive infiltration of CD8⁺ T cells into islet tumors compared to the null effects of the anti-PD-1/IgG-IL2v combination treatments (Figure 1J). The infiltrated CD8⁺ T cells were characterized by high PD-1 expression, presumably facilitating the accumulation of PD1-IL2v in the TME. Flow cytometry-based analyses confirmed the infiltration of CD8⁺ T cells into tumors upon PD1-IL2v treatment. PD1-IL2v specifically expanded the CD8⁺ T cell compartment, increasing total and TAG-specific CD8⁺ T cells up to 10-fold (Figure 1K and 1L). Consistent with the data obtained from the spleen, the total number of intratumoral Tregs was not expanded and rather slightly decreased (Figure S1C). Next, we characterized the phenotype of the CD8⁺ T cells within tumors, employing the markers and nomenclature introduced by Codarri et al.¹⁶ PD1-IL2v treatment led to a significant increase in stem-like resource PD-1⁺TCF-1⁺ CD8⁺ T cells (Figure 1M) and their progeny (PD-1⁺TCF-1⁻), especially among TAG-specific CD8⁺ T cells (Figures 1N and 1O). Next, we assessed the activation state of the infiltrating CD8⁺ T cells and identified PD-1⁺TCF-1⁻CD44⁺ effector CD8⁺ T cells, whose cytotoxic function was revealed by Granzyme B expression (Figures 1P and 1Q). We further discriminated their differentiated phenotype using the mature T cell markers CD218a and Tim-3¹⁶ and showed that PD1-IL2v elicited the expansion of “fresh” effector CD8 T cells (PD-1⁺CD218a⁺) (Figure 1R) and “better” effector CD8⁺ T cells (PD-1⁺TCF-1⁻CD218a⁺Tim-3^{high}) (Figure 1S); additionally, the proliferative phenotype of CD8⁺ T cells was increased (Figure 1T). Given the multifaceted roles of CD4⁺ T cells in anti-tumor immune responses,²⁷ we assessed their presence and phenotype but did not observe cytotoxic or proliferative CD4⁺ T cells in the TME (Figures S1D–S1E). In addition, we evaluated the formation of high endothelial venules (HEVs) on the vasculature and found that MECA-79⁺ endothelial cells displaying the features of HEVs were induced within PD1-IL2v treated tumors (Figures 1U and 1V), which we infer is facilitating CD8⁺ T cell recruitment.

PD1-IL2v treatment leads to tumor regression, although some tumors eventually relapse

Next, we evaluated the therapeutic efficacy of PD1-IL2v against established solid tumors. RT5 mice were enrolled based on tumor size, and tumor progression was longitudinally monitored by ultrasound imaging non-invasively over 16 weeks (Figure 2A). While untreated tumors continuously progressed (Figure 2B), PD1-IL2v treatment resulted in tumor regression in all mice after

two to four weeks (Figure 2C). Subsequently, 40% of mice showed complete tumor regression, whereas in the remainder, the tumors relapsed (Figures 2C and 2D). Although relapsed tumors were still infiltrated with CD8⁺ T cells (up to 30% of total cells), the number of TAG-specific CD8⁺ T cells decreased to that in untreated tumors (Figures 2E and 2F). The number of Tregs remained unaltered, and HEVs were similar to untreated controls (Figures 2G and 2H). We assessed the functional contributions of CD8⁺ and CD4⁺ T cells to therapeutic efficacy by including depleting anti-CD8 with/without anti-CD4 antibodies in PD1-IL2v-treated mice. Depleting the CD8⁺ T cells or both T cell subtypes led to a complete abrogation of the therapeutic benefit of PD1-IL2v (Figure 2I). In contrast, the depletion of the CD4⁺ T cells did not impact the survival benefit observed upon PD1-IL2v. We further characterized the CD8⁺ T cells in CD4-depleted tumors to investigate a potential helper role for CD4⁺ T cells but did not observe phenotypic differences (Figures S1F–S1J). Then, to assess the functional contribution of IFN- γ secretion by CD8⁺ T cells to the efficacy of PD1-IL2v, we used an IFN- γ -blocking antibody combined with PD1-IL2v. Blockade of IFN- γ significantly restored expansive tumor growth (Figure S1K–S1M) and abrogated HEV induction, establishing that activation of IFN- γ signaling in CD8⁺ T cells was required for the anti-tumoral responses evoked by PD1-IL2v.

To investigate acquired resistance to PD1-IL2v, islet tumors treated with PD1-IL2v were analyzed by immunofluorescence staining. While untreated islet tumors stained weakly, PD-L1 was upregulated 14 days after PD1-IL2v treatment was initiated, likely triggered by IFN- γ released by tumor-infiltrating activated CD8⁺ T cells.^{28–30} PD-L1 upregulation was further increased in relapsed tumors, most prominently on the tumor vasculature and macrophages (Figures 2J and S1N).

Anti-PD-L1 improves PD1-IL2v therapy resulting in complete tumor regression

Seeking to disrupt the adaptive resistance, we asked whether concomitant blockade of the PD-1/PD-L1 immune checkpoint pathway could improve the duration of therapeutic efficacy of PD-IL2v (Figure 3A). To reiterate, anti-PD-1 in the context of PD1-IL2v is used to deliver the bispecific molecule to tumors and is not supplied at a sufficient saturating dose to fully block PD-1 checkpoint activity. We chose to utilize PD-L1 antibody treatment instead of high-dose anti-PD-1 to circumvent competition between anti-PD-1 and PD1-IL2v for binding to PD-1 expressed on the targeted CD8⁺ T cells. Ultrasound-based imaging revealed rapid tumor regression in the first four weeks of combination therapy, whereas anti-PD-L1 monotherapy had no therapeutic benefit (Figures 3B–3D). In contrast to PD1-IL2v, where 60% of tumors relapsed, the anti-PD-L1 + PD1-IL2v combination therapy resulted in a long-lasting response without relapse in 90% of RT5 mice, leading to substantial survival benefit (Figure 3E). A complete response upon PD1-IL2v treatment combined with anti-PD-L1 is visualized in Figure 3F.

The improved efficacy of the anti-PD-L1 + PD1-IL2v combination therapy over PD1-IL2v monotherapy was further evaluated by analyzing blood glucose concentration as a biomarker. Due to the secretion of insulin by PanNET cancer cells, RT5 mice develop a hypoglycemic phenotype as the tumors progress (3–7 mmol/L). An efficacious anti-tumor therapy could be

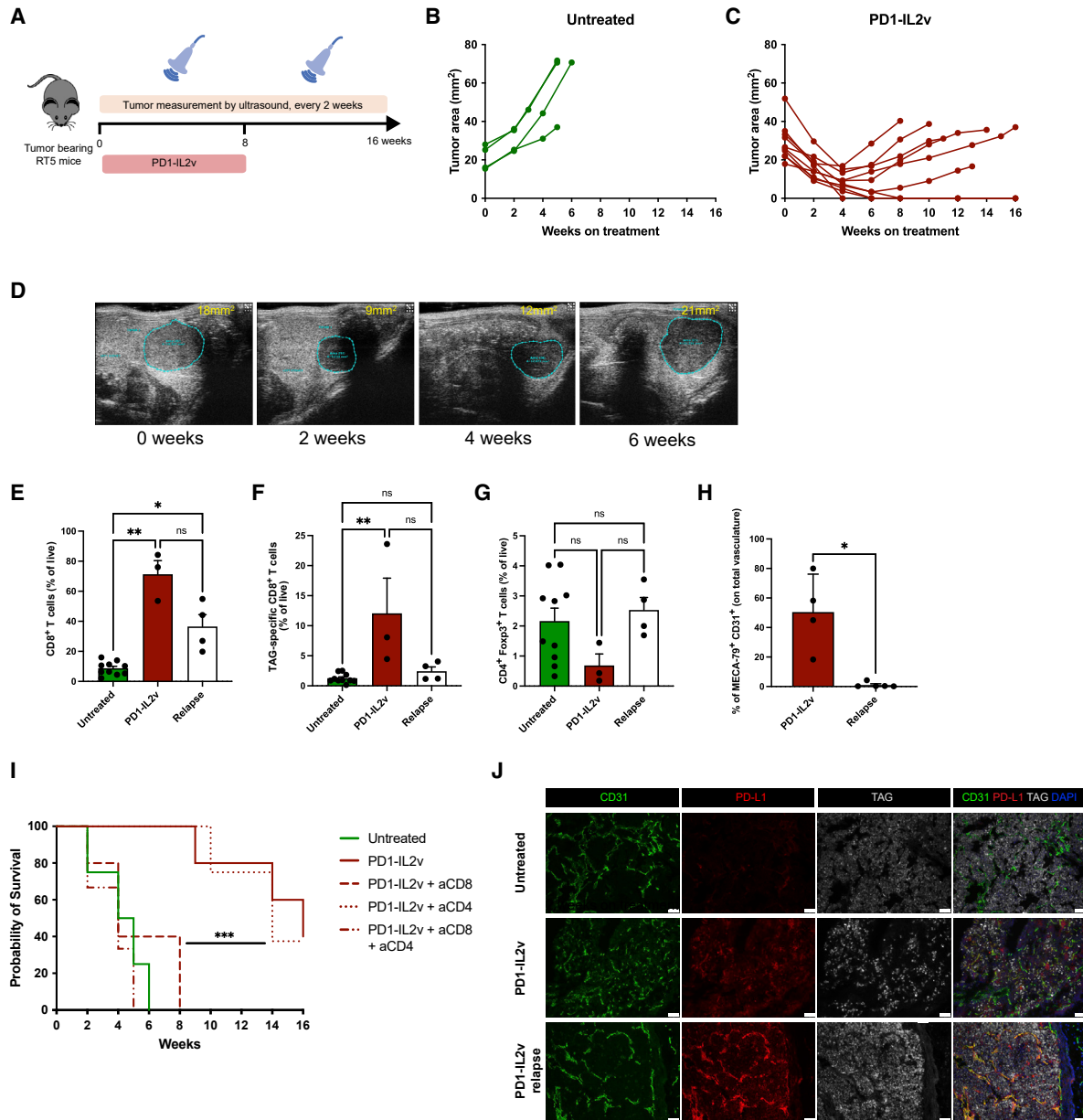


Figure 2. PD1-IL2v treatment leads to tumor regression, but some eventually relapse

(A) Schematic of long-term efficacy studies. Tumor-bearing RT5 mice were treated with PD1-IL2v for 8 weeks, and the tumor progression was monitored by ultrasound imaging for a maximum of 16 weeks.

(B) Tumor growth curves of untreated mice ($n = 4$).

(C) Tumor growth curves of RT5 mice treated with PD1-IL2v ($n = 10$).

(D) Ultrasound images of the abdomen of RT5 mice upon 0, 2, 4, and 6 weeks of PD1-IL2v treatment. Tumors are circled in blue, and the tumor area is indicated.

(E–G) Flow cytometry analyses of tumors relapsing upon PD1-IL2v compared to untreated and PD1-IL2v-treated for two weeks ($n = 3–10$). Frequency of CD8⁺ T cells (E), frequency of TAG-specific CD8⁺ T cells (F), and frequency of Foxp3⁺ CD4⁺ T cells (G).

(H) HEV quantification in the entire area of a tumor-tissue section in PD1-IL2v tumors treated for 2 weeks compared to PD1-IL2v relapsing tumors. PD1-IL2v ($n = 4$), relapse ($n = 5$).

(I) Survival graph of RT5 mice treated with PD1-IL2v and depleting antibodies for CD4 and CD8. Untreated ($n = 4$), PD1-IL2v ($n = 5$), PD1-IL2v + anti-CD8 ($n = 5$), PD1-IL2v + anti-CD4 ($n = 4$), and PD1-IL2v + anti-CD8 + anti-CD4 ($n = 3$).

(J) IF images of untreated, two weeks PD1-IL2v treated, and relapsing tumors stained for CD31, PD-L1, and TAG (scale bar, 50 μm ; $n = 4–6$).

Data in all quantitative panels are presented as mean \pm SEM.

Statistical analysis: one-way ANOVA Kruskal-Wallis with Dunn's multiple comparisons tests, Figures 2E–2G = * $p < 0.05$, ** $p < 0.01$; ns, no statistical significance. Mann-Whitney test, Figure 2H = * $p < 0.05$; ns, no statistical significance. Log rank Mantel-Cox test, Figure 2I = *** $p < 0.001$.

Please also see Figures S1F–S1N.

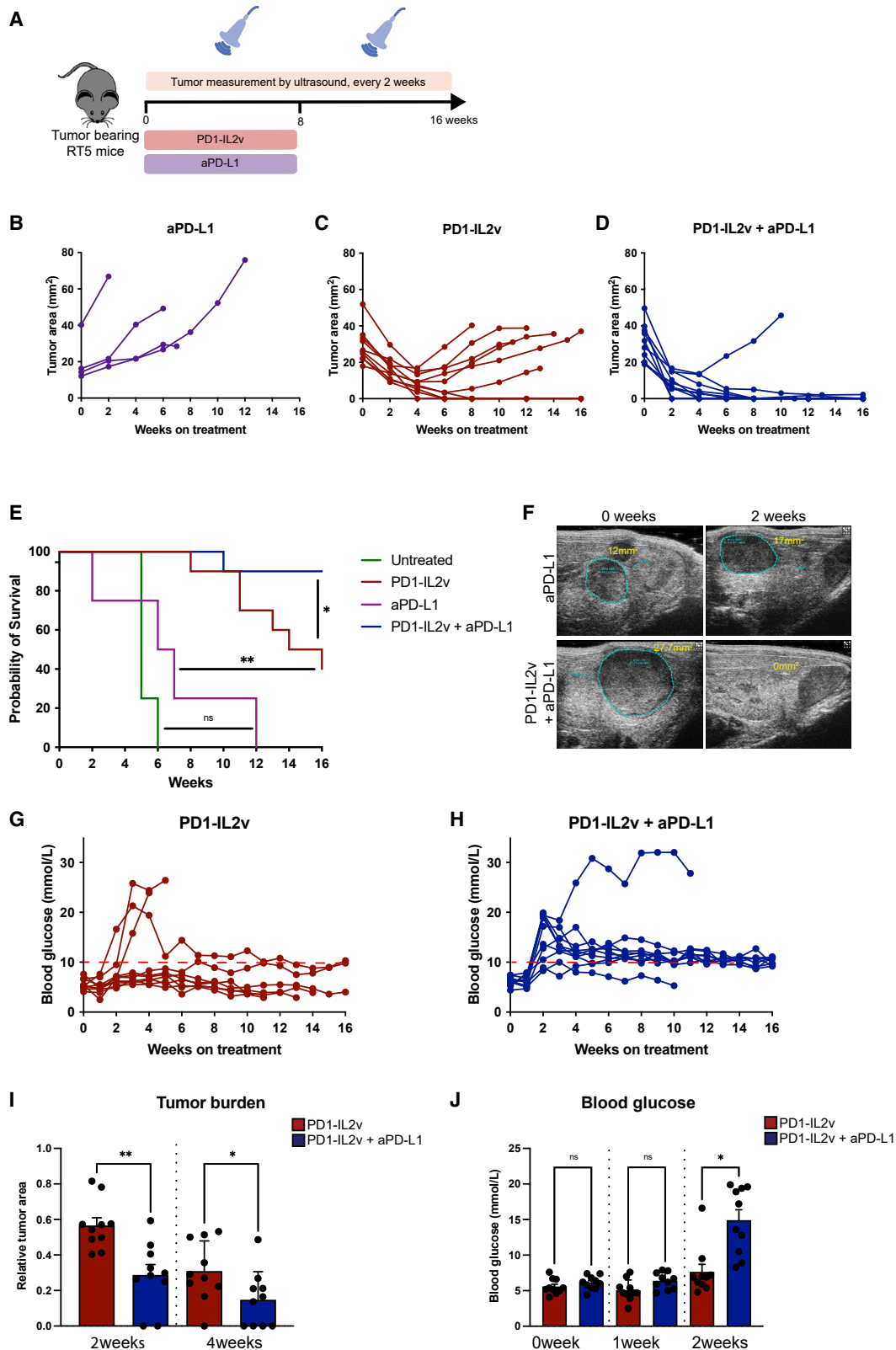


Figure 3. Anti-PD-L1 improves PD1-IL2v therapy resulting in complete tumor regression

(A) Schematic of long-term efficacy studies in RT5.

(B) Tumor growth curves of mice treated with anti-PD-L1 (n = 4).

(legend continued on next page)

envisaged to revert the hypoglycemic state to normal/hyperglycemia (10 mmol/L and above). Indeed, 40% of RT5 mice in the PD1-IL2v treatment group and 90% of the originally hypoglycemic animals treated with PD1-IL2v plus anti-PD-L1 developed and maintained normal/hyperglycemia (Figures 3G and 3H). In marked contrast, mice administered with the non-efficacious drugs, namely anti-PD-1^{low} and anti-PD-1^{high}, separately and combined with IgG-IL2v, and anti-PD-L1, all remained hypoglycemic throughout the entire treatment phase, indicative of substantial neoplastic burden (Figures S1O–S1S). These data are consistent with the ultrasound imaging, validating the superior therapeutic efficacy of PD1-IL2v + anti-PD-L1 over the other tested treatments.

Analysis of the tumor growth kinetics revealed that tumor regression was most pronounced during the first four weeks of drug administration. After two weeks of treatment, the combination of anti-PD-L1 with PD1-IL2v produced significantly greater tumor size reduction than that of PD1-IL2v monotherapy. The tumor size decreased by 70% from the initial size upon anti-PD-L1 + PD1-IL2v treatment, compared to a reduction of only 40% for the PD1-IL2v-treated mice (Figure 3I). After four weeks, tumors of the combination treatment group shrank to 15% of their starting sizes, whereas tumors treated with PD1-IL2v monotherapy showed a regression to 30% (Figure 3I). The data on the tumor volumes were corroborated by the increase in blood glucose concentration in the PD1-IL2v + anti-PD-L1 treatment group after two weeks of treatment, also indicative of PanNET shrinkage (Figure 3J).

PD1-IL2v treatment increases T cell populations both in the spleen and the TME

To investigate underlying molecular differences between PD1-IL2v monotherapy and anti-PD-L1 + PD1-IL2v combination therapy, we analyzed therapy-induced effects in the early phase of treatment when maximal tumor regression is occurring. Tumor-bearing RT5 were treated for 10 days with anti-PD-L1, PD1-IL2v or PD1-IL2v + anti-PD-L1, and spleens and tumors were subjected to single-cell RNA sequencing (scRNA-seq) and single-cell T cell receptor sequencing (scTCR-seq) (Figure 4A). Uniform Manifold Approximation and Projection (UMAP)-based clustering analyses of scRNA-seq data of spleen samples revealed a 2-fold increase in CD8⁺ T cells and natural killer (NK) cells in both PD1-IL2v treatment groups compared to untreated and anti-PD-L1-treated mice (Figures S2A, S2B, and Table S1).

In particular, a CD8⁺ T cell cluster (CD8_2) with characteristics of effector-memory (EM) cells (Figures S2B–S2D) was specifically expanded upon PD1-IL2v treatment. The number of distinct splenic cell populations involving the T cell compartment was unaltered upon combining PD1-IL2v with anti-PD-L1 (Figures S2B and S2E–S2H), nor was CD8⁺ T cell proliferation affected (Figure S2I). In contrast, the draining lymph nodes contained more proliferating CD8⁺ T cells, and an expansion of antigen-specific resource stem-like cells, but not of their progeny (Figures S2J–S2L).

Next, we analyzed scRNA-seq datasets from RT5 tumor samples from the four different treatment conditions. UMAP-based clustering identified major clusters that were assignable to distinct cell populations by their gene expression profiles (Figures 4B and S3). Quantification of these distinct cell populations revealed that untreated tumors consisted primarily of cancer cells (>50%), followed by macrophages (20%) (Figure 4C and Table S2). The T cell compartment accounted for around 6% of all cells in untreated tumors. Treatment of mice with PD1-IL2v resulted in a pronounced expansion of the T cell compartment, with CD8⁺ and CD4⁺ T cells collectively constituting more than 80% of cells within the tumor, confirming our results obtained by flow cytometry and immunofluorescence (IF) imaging. The combination of PD1-IL2v with anti-PD-L1 did not lead to significant changes in cell-type abundances in the TME compared to PD1-IL2v monotherapy (Figures 4C and 4D). Anti-PD-L1 monotherapy, in contradistinction, had distinctive effects: the cancer cells decreased to 34%, and T cells increased to 35% compared to untreated tumors. B cells were increased 4- to 5-fold in tumors treated with anti-PD-L1 compared to untreated controls, whereas cancer-associated fibroblasts (CAFs) were reduced, and the abundance of macrophages was unaltered. Notably, the percentage of macrophages and CAFs were both reduced in the cohorts treated with PD1-IL2v with/without PD-L1 (Figures 4C and 4D).

PD1-IL2v with/without anti-PD-L1 treatment expands effector memory CD8⁺ T cells with better effector function compared to anti-PD-L1

We next characterized the CD8⁺ T cells present within the tumors upon PD1-IL2v + anti-PD-L1 compared to untreated and PD1-IL2v monotherapy (Figures S4A–S4E). The addition of anti-PD-L1 did not impact or potentiate the phenotypic effects of PD1-IL2v, as we observed a similar phenotype and number

(C) Tumor growth curves of mice treated with PD1-IL2v (same figure as Figure 2C).

(D) Tumor growth curves of mice treated with PD1-IL2v combined with anti-PD-L1 (n = 10).

(E) Survival graph of the different treatment groups. Two mice in the PD1-IL2v and one in the PD1-IL2v + anti-PD-L1 treatment group developed severe hyperglycemia due to the complete response and had to be euthanized before the end of the 16-week treatment period. These mice were still considered complete responders in the graph. The data of the untreated and mice treated with PD-IL2v have been previously reported in Codarri et al. 2022.¹⁶

(F) Ultrasound images of the abdomen of RT5 mice before (t = 0) and after two weeks of anti-PD-L1 and PD1-IL2v + anti-PD-L1 treatment. The tumors are circled in blue, and the tumor area is indicated.

(G and H) Blood glucose concentration upon PD1-IL2v treatment (G) and upon PD1-IL2v + anti-PD-L1 treatment (H) (n = 10). Normal glucose concentrations in healthy, non-transgenic littermates are indicated by the dashed red line.

(I) Relative tumor burden of PD1-IL2v and PD1-IL2v + anti-PD-L1-treated mice after 2 or 4 weeks of treatment.

(J) Blood glucose concentration of PD1-IL2v and PD1-IL2v + anti-PD-L1-treated mice at the start of treatment (week 0) and after 1 or 2 weeks of treatment.

Data in all quantitative panels are presented as mean ± SEM. The data of the long-term studies are pooled from 2–3 independent experiments. Statistical analysis: log rank Mantel-Cox test, Figure 4E = *p < 0.05 (PD1-IL2v vs. PD1-IL2v + anti-PD-L1), **p < 0.01 (anti-PD-L1 vs. PD1-IL2v), ns (untreated vs. anti-PD-L1). One-way ANOVA Kruskal-Wallis with Dunn's multiple test (comparing matching weeks), Figures 4I and 4J = *p < 0.05, **p < 0.01.

Please also see Figures S1O–S1S.

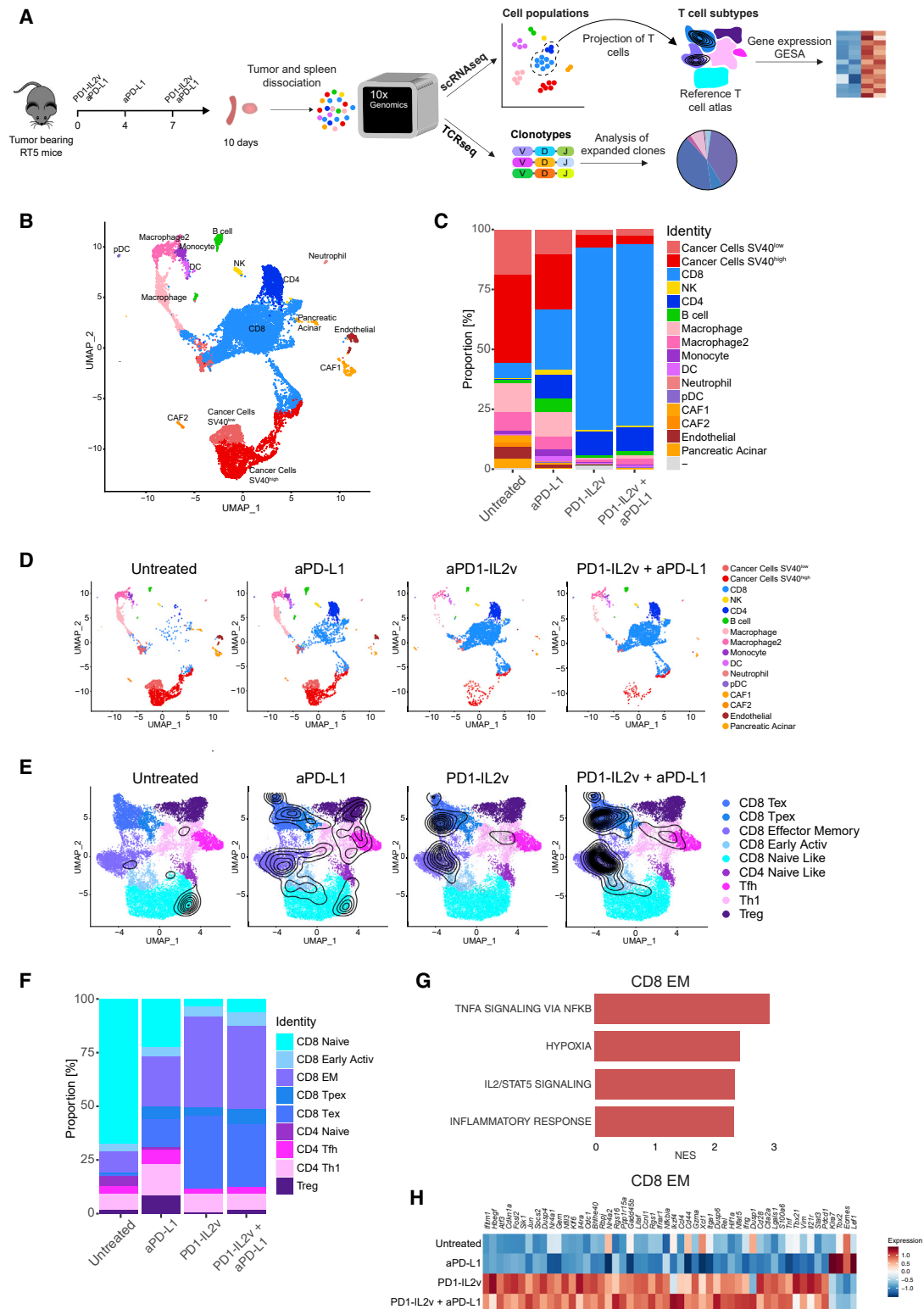


Figure 4. PD1-IL2v treatment increases intratumoral T cell populations

(A) Tumor-bearing RT5 mice were left untreated or treated with anti-PD-L1, PD1-IL2v, or PD1-IL2v + anti-PD-L1 for 10 days, and spleen and tumor samples were subjected to single-cell RNA and TCR sequencing and subsequent bioinformatic analyses.

(B) UMAP plot of merged datasets showing distinct cell populations in RT5 tumors.

(C) Proportion of the distinct cell populations.

(legend continued on next page)

of CD8⁺ T cells, and the CD4⁺ T cells remained unaltered (Figures S4F and S4G). The numbers of total and TAG-specific CD8⁺ T cells, stem-like resource PD-1⁺TCF1⁺, effector (PD-1⁺CD218a⁺ and PD-1⁺TCF-1⁻CD218a⁺Tim-3^{high}), cytotoxic (GZMB⁺) and proliferative Ki67⁺ CD8⁺ T cells were not altered when anti-PD-L1 was added to PD1-IL2v (Figures S4A–S4E).

Furthermore, the scRNA-seq-based transcriptome data of both CD4⁺ and CD8⁺ T cells were selected and analyzed by ProjectTILs. In this approach, T cells are projected onto a reference atlas created by different published datasets consisting of 25 samples compiled from 6 different studies.³¹ Using this algorithm, T cells are assigned to “functional clusters” characterized by known gene expression signatures of specific T cell subtypes: naive-like CD8⁺ T cells (naive/central memory cells); EM CD8⁺ T cells; “early-activation” CD8⁺ T cells (intermediate profile between naive-like and EM); CD8⁺ precursor-exhausted cells (Tpex, equal to stem-like resource cells); CD8⁺ terminally-exhausted (Tex) effector cells; CD4⁺ Th1-like cells, CD4⁺ follicular-helper (Tfh); and Tregs.

The projection of the four treatment groups onto the ProjectTILs reference atlas is displayed in Figure 4E and quantified in Figure 4F. The expression of diagnostic T cell markers in the distinct T cell populations is shown in Figures S5A–S5I. In untreated tumors, the majority of CD8⁺ T cells were classified as having a naive-like subtype, whereas 14% had an EM-like subtype. In the anti-PD-L1 treatment group, the EM subtype as well as the exhausted CD8⁺ T cell subtype were expanded compared to untreated tumors. In addition, anti-PD-L1 treatment resulted in a 2-fold expansion of the Th1 subtype and a 4-fold increase in Tregs in comparison to untreated controls. In contrast, tumors treated with PD1-IL2v were characterized by an abundance of EM CD8⁺ T cells, accounting for more than 40% of all T cells. The second most abundant T cell population in the PD1-IL2v treated tumors projected to the exhausted CD8⁺ T cell subtype (Tex), representing around 35% of all T cells. Importantly, Tregs were decreased upon PD1-IL2v treatment compared to anti-PD-L1 treated tumors, confirming that the mutated version of IL2v does not induce Tregs. Substantiating the analyses above, there were no significant changes in the percentages of T cell subtypes in the PD1-IL2v + anti-PD-L1 combination treatment compared to PD1-IL2v monotherapy (Figure 4F).

We then investigated the functional states of the CD8⁺ T cell subsets using gene enrichment analyses of the scRNA-seq datasets, comparing anti-PD-L1 monotherapy to anti-PD-L1 + PD1-IL2v. EM CD8⁺ cells showed IL2-Stat5 and TNF-A signaling pathway enrichment, indicating the PD1-IL2v treatment was resulting in the generation of better effector CD8⁺ T cells compared to anti-PD-L1 treatment (Figure 4G and Table S3); the EM CD8⁺ T cells displayed higher expression of genes involved in T cell activation (*Ctla2a*, *Xcl1*, and *Cd44*) and cytotoxicity (*Gzmba* and *Tnf*), whereas genes involved in T cell inactivation (*Tox2*

and *Eomes*) were repressed (Figure 4H). Similarly, increased expression of *Gzmba*, *Tnf*, and *Ctla2a* were maintained, and TNF-A and IL2-Stat5 signaling pathways were enriched in CD8⁺ Tex upon PD1-IL2v treatment compared to anti-PD-L1 (Figures S5J and S5K), indicating the CD8⁺ Tex subtype in the PD1-IL2v treatment groups were not terminally exhausted and therefore dubbed as “pseudo-exhausted.” Comparison of PD1-IL2v + anti-PD-L1 with PD1-IL2v treatment revealed no major pathway changes within CD8⁺ T cell populations, based on global gene expression profiles and signaling pathway enrichment. These results strengthen our previous data: the addition of anti-PD-L1 on top of PD1-IL2v does not impact the cell differentiation status of the T cell compartment.

Taken together, the data from the scRNA-seq confirmed the extensive expansion of CD8⁺ T cells in RT5 tumors treated with PD1-IL2v with/without anti-PD-L1. The expanded CD8⁺ T cells primarily consisted of EM and pseudo-exhausted T cells, which are inferred to have better effector function compared to anti-PD-L1 treatment based on gene expression analysis. These data agree with the flow cytometry-based analyses identifying CD8⁺ T cells with better effector function upon PD1-IL2v treatment (Figures 1K–1T and S4A–S4E).

PD1-IL2v synergizes with anti-PD-L1 to elicit clonal T cell expansion with increased diversity

To investigate changes in the TCR repertoire of intratumoral T cells in the different treatment groups, scTCR-seq was employed (Figure 4A). In untreated tumors, TCR sequences could be detected in 50% of T cells (Figure 5A). In the other treatment groups, over 80% of T cells contained TCR sequences (Figure 5A). Although the richness of the TCR repertoire in the three treatment groups was similar (Figure S6A), the total number of clones in tumors treated with PD1-IL2v with/without anti-PD-L1 was higher compared to anti-PD-L1-treated samples, suggesting a clonal expansion of antigen-specific T cells in the PD1-IL2v treatment groups (Figure 5B).

Analysis of TCR diversity revealed an increase upon anti-PD-L1 treatment (Figure 5C), markedly more so than for PD1-IL2v monotherapy. TCR diversity was elevated to an intermediate extent when anti-PD-L1 was combined with PD1-IL2v, substantiating that anti-PD-L1 treatment adds diversity to the TCR repertoire. Next, the proportion of the distinct clonotypes was determined (Figure 5D). In untreated tumors, the majority of T cell clones were only represented once, and only a few clonotypes were expanded. Similarly, in tumors treated with anti-PD-L1, ~50% of the T cell clones were only present once. In contrast, in both PD1-IL2v treatment groups, more than 50% of T cell clones were expanded and found more than 10 times. The similarity of the two PD1-IL2v treatment groups was confirmed by correlation analyses of the V and J gene usage (Figure S6B). To investigate whether tumor antigen-specific T cell clones were expanded upon PD1-IL2v treatment, we

(D) Individual UMAP plot displaying distinct cell populations.

(E) Projection of T cells (black profile) onto a reference T cell atlas from ProjectTILs (colored T cell subtypes).

(F) Proportion of T cell subtypes defined by the reference T cell atlas in Figure 4E.

(G) Hallmark gene enrichment analysis comparing gene expression profiles of CD8⁺ EM T cells of PD1-IL2v + anti-PD-L1 to anti-PD-L1 treatment.

(H) Expression of selected immune-related genes in CD8⁺ EM T cells represented as a heatmap. N = 2 for all treatment groups.

Please also see Figures S2, S3, S4, S5, Tables S2, and S3.

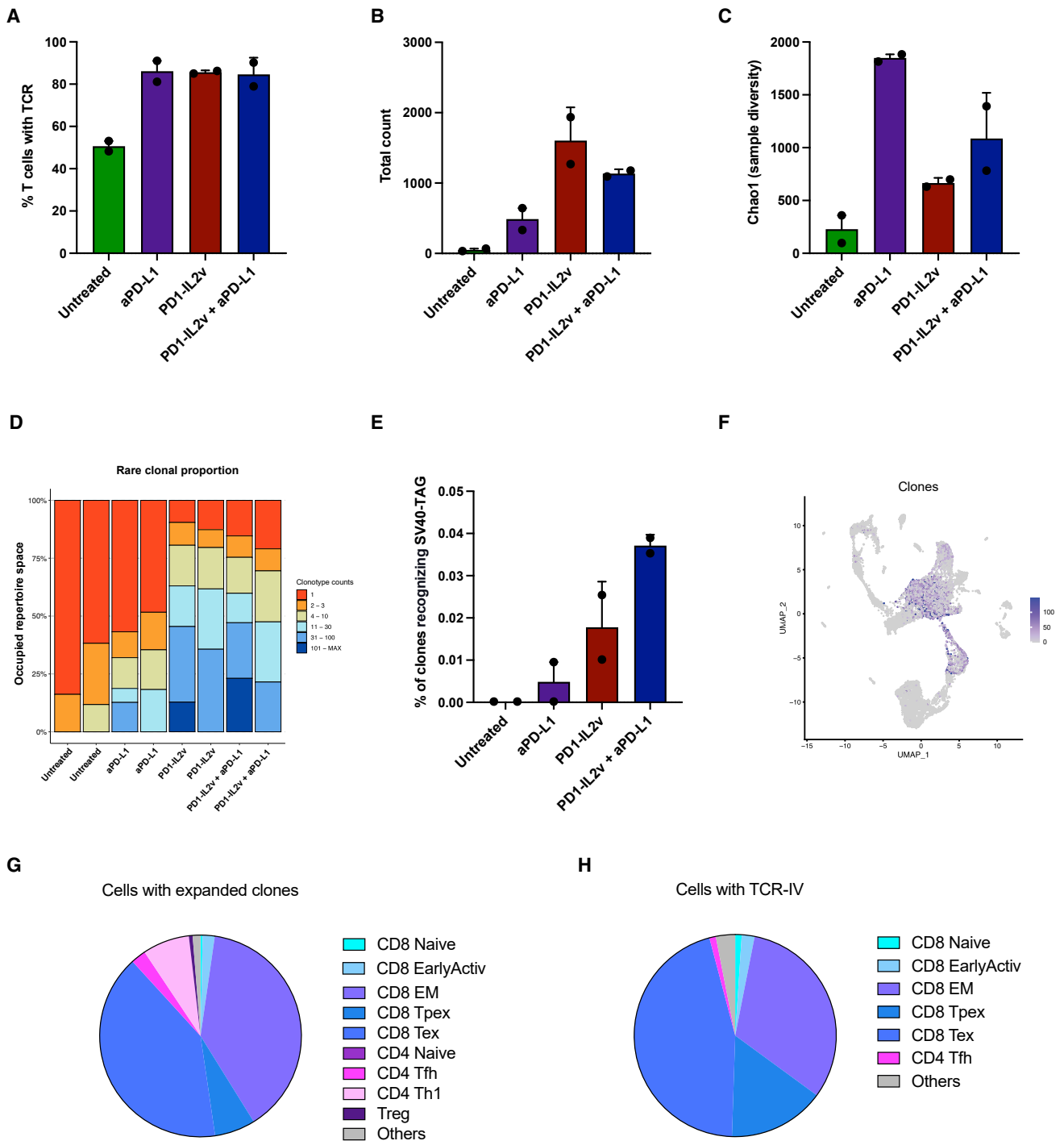


Figure 5. PD1-IL2v synergizes with anti-PD-L1 resulting in clonal T cell expansion with increased diversity

Tumor-bearing RT5 mice were treated as described in Figure 4A.

(A) Percentage of T cells in the scRNA-seq analysis containing detectable TCR expression.

(B) Total counts of TCRs.

(C) Chao1 diversity estimation.

(D) Proportion of clonotypes with specific counts ranging from single counts to clonotypes with more than 101 counts.

(E) Proportion of clones recognizing two known SV40 TAG immunogenic epitopes (TCR-I and TCR-IV).

(F) UMAP colored by counts of clones with the same clonotype per cell.

(G) Proportion of expanded clones (found more than 5 times) identified in the distinct T cell populations.

(H) Proportion of the SV40 TAG clone TCR-IV in the distinct T cell populations. N = 2 for all treatment groups.

Please also see Figure S6.

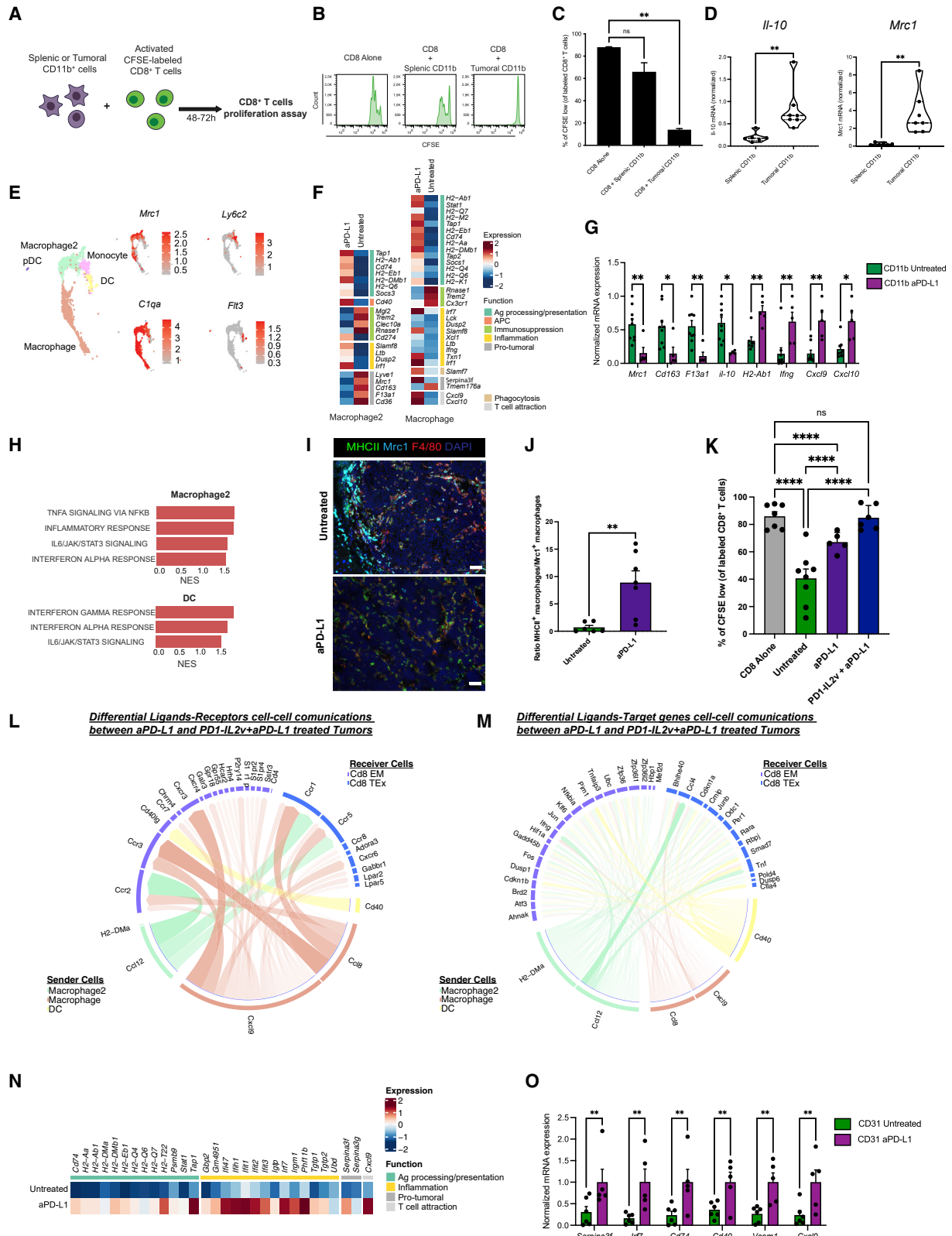


Figure 6. Reshaping of macrophages by anti-PD-L1 and its complementarity with PD1-IL2v

(A) Schematic of T cell proliferation assay of *in vitro*-activated splenic T cells in the presence of splenic or tumoral CD11b⁺ myeloid cells. (B) Histogram showing T cell proliferation alone or in the presence of splenic or tumoral myeloid cells (n = 6–7).

(legend continued on next page)

considered two known T cell receptors (TCR-I and TCR-IV) recognizing SV40 TAG epitopes that had been previously identified in mouse models expressing SV40 TAG.^{32–34} We found that T cell clones harboring these TCRs were expanded in the PD1-IL2v group and further increased upon PD1-IL2v + anti-PD-L1 treatment (Figure 5E).

Expanded T cell clones identified more than five times in tumors were primarily associated with the better effector CD8⁺ EM and pseudo-exhausted CD8⁺ Tex cell populations (Figures 5F, 5G, and S6C–S6E). Moreover, expanded T cell clones displaying TCR-IV recognizing the SV40 Tag tumor antigen were well represented in T_{pex} cells, in better effector CD8⁺ T-EM cells, and in pseudo-exhausted CD8⁺ Tex cells (Figure 5H). Collectively, the TCR repertoire analysis revealed that PD1-IL2v resulted in the expansion of T cell clonotypes, whereas anti-PD-L1 treatment increased TCR diversity. The enhanced TCR diversity produced by anti-PD-L1 is envisaged to contribute to the improved therapeutic efficacy observed with the anti-PD-L1 + PD1-IL2v combination.

Anti-PD-L1 reshapes the intratumoral macrophages and complements PD1-IL2v to improve anti-tumor immunity

To better understand the impact of combining anti-PD-L1 with PD1-IL2v, we investigated the effect of anti-PD-L1 alone. We focused on myeloid cells, which are known to regulate anti-tumor responses by directly or indirectly modulating T cell functions in the TME.³⁵ Among these, macrophages have diverse activities; in many cancers, tumor-associated macrophages (TAMs) are tumor-promoting and associated with immunosuppression, and a previous study implicated anti-PD-L1 in modulating TAM phenotypes.³⁶ We therefore performed *ex vivo* assays wherein tumoral or splenic myeloid cells were co-cultured with activated CD8⁺ T cells to assess T cell proliferation. Tumor-derived CD11b⁺ myeloid cells, but not splenic myeloid cells, exhibited direct immunosuppressive activity on *in vitro* activated splenic CD8⁺ T cell proliferation (Figures 6A–6C). Furthermore, we identified an M2-

like Mrc1⁺ TAM population within the CD11b⁺ compartment that expressed the immunosuppressive cytokine IL-10 in untreated tumors but not in cognate spleens (Figure 6D).

scRNA-seq analyses of myeloid cells (Figure 6E) revealed that anti-PD-L1 treatment was selectively impacting the phenotype and function of TAMs, polarizing the TAMs toward a pro-inflammatory and antigen-presenting-cell (APC)-like phenotype that could logically participate in the recruitment of T cells. Indeed, we observed a reduction in M2-like immunosuppressive markers, such as *Trem2*, *Mrc1*, and *Cd163*,^{35,37} and upregulation of pro-inflammatory macrophage markers, such as *Irf1*, *Slamf8*, and *Irfng* and the T cell attractant chemokines *Cxcl9* and *Cxcl10*. Furthermore, we observed an increase in antigen-processing and -presenting genes, such as *Cd74*, *Tap1*, and *H2-Ab* (Figure 6F). We validated these results by performing gene expression analyses on myeloid cells isolated from untreated and anti-PD-L1-treated tumors (Figure 6G). Interestingly, IL6, TNF α , and inflammatory signaling pathways were enriched in the PD1-IL2v plus anti-PD-L1 combination treatment arm compared to PD1-IL2v alone, both in the macrophage-2 and DC clusters (Figure 6H and Table S3). Moreover, we examined both *Mrc1* and MHC class II expression in macrophages via immunostaining of tumor sections, which confirmed the switch from an immunosuppressive (*Mrc1*) to a more pro-inflammatory (MHC-II) phenotype in response both to anti-PD-L1 monotherapy and in combination with PD1-IL2v (Figures 6I, 6J, and S7A–S7F). To functionally assess the inferred reprogramming of TAMs, we performed an *ex vivo* co-culture assay, revealing that myeloid cells isolated from the untreated tumors suppressed CD8⁺ T cell proliferation, whereas myeloid cells from the anti-PD-L1 group were significantly less suppressive (Figure 6K).

Using Nichenet, an algorithm for mapping cell-cell communications in scRNA-seq datasets,³⁸ we charted differentially increased ligand-receptor pairs in anti-PD-L1 vs. anti-PD-L1 + PD1-IL2v treated tumors, querying ligands expressed in myeloid cells (Macrophage, Macrophage2, and DCs) as “senders” and

(C) Quantification of T cell proliferation as CFSE^{low} CD8⁺ T cells (n = 6–7).

(D) *Il-10* and *Mrc1* expression on splenic and tumoral myeloid cells.

(E) Myeloid cell compartment in the RT5 scRNA-seq dataset (from Figure 4B), highlighting distinct myeloid cell populations and markers (*C1qa*-Macrophage, *Mrc1*-Macrophage2, *Ly6c2*-Monocyte, and *Fit3*-DC).

(F) Gene expression heatmap of two clusters of intratumoral macrophage populations (macrophage 2 and macrophage) in the scRNA-seq dataset, comparing untreated to anti-PD-L1 treatment. The genes are grouped by function.

(G) mRNA-expression analyses of tumoral myeloid cells isolated from untreated and anti-PD-L1-treated RT5 mice after 10 days. Untreated (n = 9), anti-PD-L1 (n = 5).

(H) Gene enrichment analysis of scRNA-seq dataset in macrophage 2 and DC populations comparing PD1-IL2v + anti-PD-L1 vs. PD1-IL2v treatment.

(I) IF images for *Mrc1*, MHCII, and F4/80 in RT5 tumors treated for 10 days (scale bar, 50 μ m).

(J) Ratio of M1-like MHCII⁺F4/80⁺ to M2-like *Mrc1*⁺F4/80⁺ macrophages quantified from the IF staining. Untreated (n = 6), anti-PD-L1 (n = 7).

(K) *Ex vivo* co-culture of isolated tumoral CD11b cells and activated splenic CFSE-labeled CD8⁺ T cells alone (n = 7), untreated (n = 8), or treated with anti-PD-L1 (n = 5) or PD1-IL2v + anti-PD-L1 (n = 6).

(L) Inferred cell-cell communication networks from myeloid cells as senders of ligands to CD8⁺ T cells as receivers expressing cognate receptors in PD1-IL2v + anti-PD-L1 tumors.

(M) Inferred cell-cell communication networks from myeloid cells as senders of ligands to CD8⁺ T cells as receptor-expressing receivers showing active target genes induced in PD1-IL2v + anti-PD-L1 tumors.

(N) Gene expression heatmap of the intratumoral endothelial cell compartment in the scRNA-seq dataset comparing untreated to anti-PD-L1 treatment. The genes are grouped by function.

(O) mRNA expression analyses of endothelial cells isolated from untreated and anti-PD-L1-treated RT5 mice for 10 days. Untreated (n = 6), anti-PD-L1 (n = 5). Data in all quantitative panels are presented as mean \pm SEM.

In vitro assays were independently repeated at least twice, and each dot represents the average of two or three technical replicates.

Statistical analysis: two-way ANOVA, Figures 6C, 6G, 6O, and 6K = *p < 0.05, **p < 0.01, ****p < 0.0001; ns, no statistical significance; Mann-Whitney test, Figure 6D = **p < 0.01.

Please also see Figures S7A–S7G and Tables S2 and S3.

receptors expressed in CD8⁺ T cells (EM and T_{pex}) as “receptors” (Figure 6L). Among the identified ligands, *Cxcl9* and *H2-DMA* were upregulated in myeloid cells upon anti-PD-L1 treatment (Figure 6F) and implicated by the cell-cell communication analysis to interact with their cognate receptors expressed by the CD8⁺ T cells (Figure 6L). Furthermore, analyses of the cell-cell communication between the myeloid senders to the CD8⁺ T receivers revealed activation of specific CD8⁺ T cell target genes such as *Ifng*, *Ccl4*, and *Atf3* already associated via the ProjectTILs analyses to the T cell-mediated anti-tumor response (Figures 6L, 6M, and 4H). Although anti-PD-L1 did not affect HEV formation (Figure S7G), scRNA-seq analyses of endothelial cells (Figure 6N) revealed that anti-PD-L1 treatment impacted the phenotype and function of the tumor vasculature, biasing it toward a pro-inflammatory and APC-like state that is envisaged to facilitate recruitment and infiltration of T cells. We extended these results by performing gene expression analyses on tumoral-derived endothelial cells isolated from untreated and anti-PD-L1-treated tumors (Figure 6O).

PD1-IL2v and anti-PD-L1 combinatorial activity on T cells and the TME is mechanistically recapitulated in a mouse model of glioma

To begin assessing the immunostimulatory effect of PD1-IL2v and its combination with anti-PD-L1 in other tumor types, we used the syngeneic GL261 orthotopic transplant model^{39,40} (Figure 7A). Treatment of glioma-tumor-bearing mice with PD1-IL2v monotherapy reduced tumor growth in short-term trials (Figure 7B) and induced CD8⁺ T cell infiltration, which was sustained in the combination (Figures 7C and 7D) as shown by MRI imaging (Figure S7H). Next, we characterized the phenotype of CD8⁺ T cells within these brain tumors and found that treatment with PD1-IL2v + anti-PD-L1 significantly increased stem-like resource (PD-1⁺TCF-1⁺) CD8⁺ T cells as well as their progeny (PD-1⁺TCF-1⁺) and effector CD8⁺ T cells (Figures 7E–7H).

Furthermore, we investigated the impact of anti-PD-L1 on macrophages. Similar to the RT5 model, we observed fewer M2-like Mrc1⁺ macrophages in the glioma tumors (Figures 7I and 7J). Gene expression analyses of myeloid cells isolated from untreated and anti-PD-L1-treated tumors revealed an increase in antigen processing and presenting genes such as *Cd40*, *H2-Aa*, and *H2-Ab1* (Figure 7K), as well as the T cell attractant chemokines *Cxcl9* and *Cxcl10*. Finally, the myeloid cells isolated from untreated and PD1-IL2v-treated glioma tumors suppressed CD8⁺ T cell proliferation (Figure 7L). In contrast, those from anti-PD-L1 and PD1-IL2v + anti-PD-L1-treated tumors were significantly less inhibitory (Figure 7L), as in the RT5 PanNET model. Moreover, we performed transcriptional profiling of endothelial cells isolated from PD1-IL2v + anti-PD-L1-treated tumors and observed increased expression of the pro-inflammatory markers *Vcam1*, *Cd40*, and *Irf7* (Figures S7I–S7K). Taken together, the results in the glioma model recapitulate the immunostimulatory functions of PD1-IL2v on CD8⁺ T cells and the reprogramming of immunostimulatory macrophages by anti-PD-L1.

DISCUSSION

Herein, we evaluated the molecular, cellular, and therapeutic effects of PD1-IL2v, an innovative immunotherapeutic agent, in the

RT5 mouse model of PanNET. We show that the PD1-IL2v bifunctional immunocytokine produces significant therapeutic efficacy that can be further improved in synergistic combination with anti-PD-L1.

Our data suggest that PD1-IL2v expands pre-existing tumor antigen-specific CD8⁺ T cells infiltrating solid tumors. Such antigen-experienced CD8⁺ T cells have not been previously reported in PanNETs of RT5 mice, and tumors in this model have instead been described as “immune deserts.”²³ It is possible that the different genetic backgrounds of the RT5 mice used historically (FVBN) vs. the current study (C57BL6/N) could be a factor. The present study established that PD1-IL2v treatment expands tumor antigen-specific CD8⁺ T cells with a stem-like phenotype of “resource T cells” and their derivative cytotoxic effector progeny, as elaborated in-depth in a recent report.¹⁶ Moreover, Ren et al. recently reported the reactivation of dysfunctional tumor-specific CD8⁺ T cells when employing a similar anti-PD1-IL2 immunocytokine.⁴¹ Our data support a model by which CD8⁺ T cells become dysfunctional during tumor progression through sustained tumor antigen exposure and modulation by the immunosuppressive TME.^{42,43} Importantly, we demonstrate that tumor-specific CD8⁺ T cells remain in a stem-like state of “resource cells” in solid tumors and are expanded upon PD1-IL2v treatment, but not by anti-PD-1 or anti-PD-L1 ICB. Notably, the presence of intratumoral stem-like CD8⁺ T cells has been proposed to be an instrumental sub-population that is expanded upon immune checkpoint treatments and correlated with response to ICB in cancer patients.^{2,20,44} Moreover, both tumor-infiltrating and systemic CD8⁺ T cells have been implicated in efficacious immunotherapy,^{20,45–48} consistent with our observations following PD1-IL2v treatment.

Established islet tumors developing in the RT5 model have been shown to exhibit resistance toward tumor-antigen vaccines and immune-checkpoint inhibitors.^{23,25,26} The tumor vasculature has been implicated as a barrier limiting the efficacy of such immunotherapies in this model,^{23,24,28} and modulation of the tumor vasculature,^{49,50} including the induction of HEVs, improved the trafficking of CD8⁺ T cells into the tumors and the efficacy of immunotherapies.^{26,51–54} In addition, tumor-associated macrophages have been implicated as another immunosuppressive barrier present in this model; notably, targeting macrophages with low dose irradiation resulted in improved therapeutic efficacy of immunotherapies.⁵⁵ Interestingly, both inflammatory barriers in the RT5 mouse model can evidently be transiently circumvented by the bispecific PD1-IL2v molecule without the necessity of tumor antigen vaccination, adoptive cell transfer, or other modulations of the TME. In tumors relapsing after PD1-IL2v treatment, we identified upregulation of PD-L1 on tumor-infiltrating macrophages and tumor vasculature as a possible mechanism of acquired resistance and then demonstrated that co-targeting with anti-PD-L1 synergistically improved the efficacy of PD1-IL2v, evidently disrupting the PD-L1-mediated resistance mechanism that re-established both inflammatory barriers.

Untreated tumors were infiltrated with “M2-like” macrophages that were replaced or reprogrammed by anti-PD-L1 into pro-inflammatory TAMs with antigen-processing and antigen-presenting gene signatures, which evidently participated in T cell recruitment. These results are consistent with a proposed mechanism^{36,56–59} whereby blockade of PD-L1

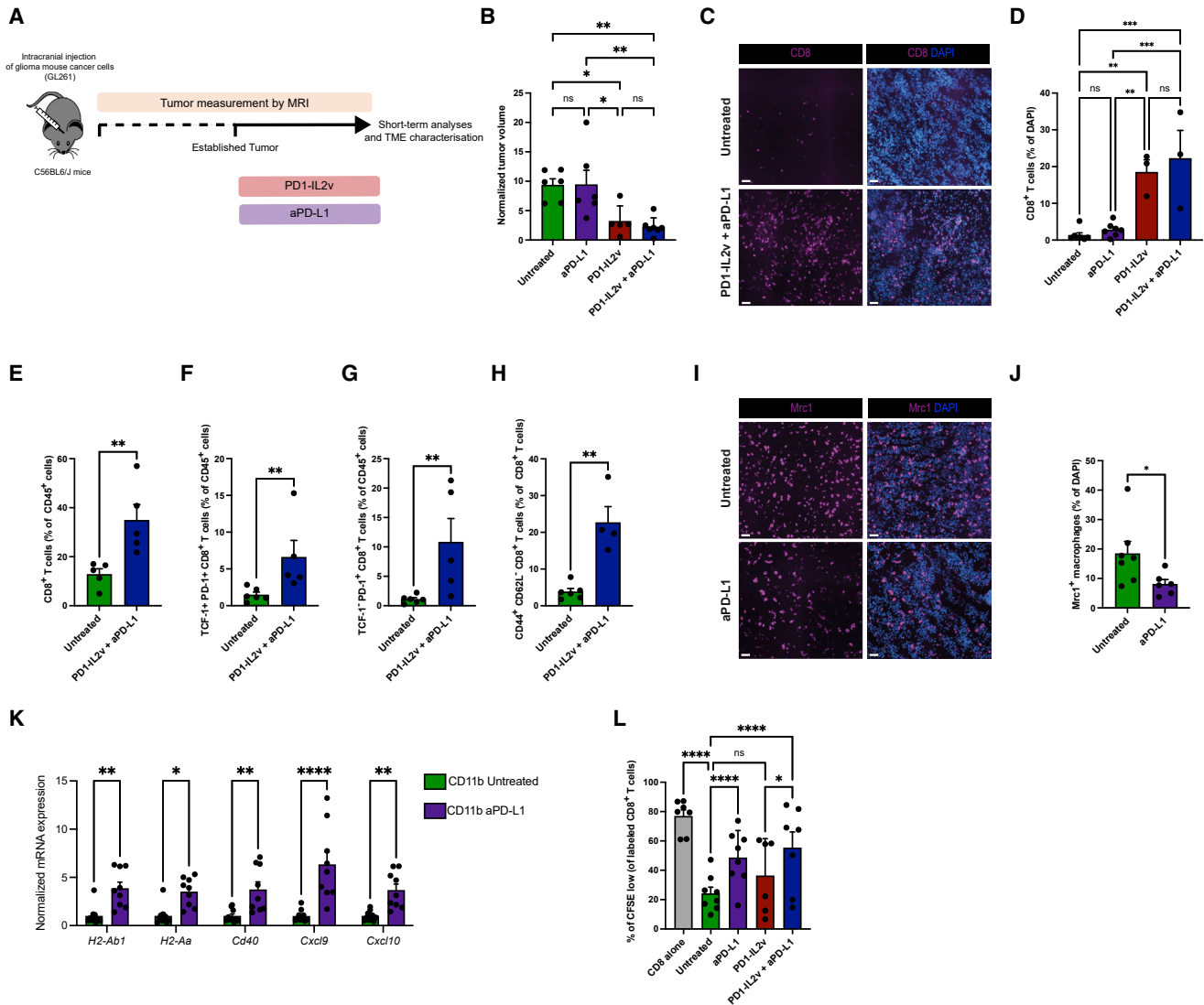


Figure 7. Stem-like T lymphocytes are expanded by PD1-IL2v in a mouse model of glioma, and anti-PD-L1 induces remodeling of macrophages

(A) Schematic of the short-term studies in an orthotopic syngeneic mouse model of glioma (GL261 cell line).

(B) Normalized tumor volume in mice treated for 10 days.

(C) IF images for CD8 in GL261 tumors subjected to the indicated treatment for one week (scale bar, 50 μ m).

(D) Quantification of CD8⁺ T cells in GL261-treated tumors.

(E–H) Flow cytometry analysis of intratumoral CD8⁺ T cells (E), stem-like CD8⁺ T cells (F), progeny CD8⁺ T cells (G), and CD62L⁻CD44⁺ effector T cells (H).

(I) IF image for Mrc1 (purple) in a treated GL261 tumor. (Scale bar, 50 μ m).

(J) Quantification of Mrc1⁺ macrophages in GL261-treated tumors. Untreated (n = 7), anti-PD-L1 (n = 6).

(K) mRNA expression analyses of tumoral myeloid cells isolated from untreated and anti-PD-L1 treated tumors. Untreated (n = 10), anti-PD-L1 (n = 9).

(L) *Ex vivo* co-culture of isolated tumoral CD11b⁺ cells and activated splenic CFSE-labeled CD8⁺ cells. Each dot represents the average of two or three technical replicates. T cells alone (n = 12), untreated (n = 8), and treated with anti-PD-L1 (n = 8), PD1-IL2v (n = 6), PD1-IL2v + anti-PD-L1 (n = 7).

For IF analyses: untreated (n = 7), anti-PD-L1 (n = 7), PD1-IL2v (n = 3), PD1-IL2v + anti-PD-L1 (n = 3).

Data in all quantitative panels are presented as mean \pm SEM.

Experiments were independently repeated at least twice.

Statistical analysis: one-way ANOVA Kruskal-Wallis with Dunn's multiple test, Figures 7B and 7D = *p < 0.05; **p < 0.01; Mann-Whitney, Figures 7E–7H and 7M = *p < 0.05, **p < 0.01; two-way ANOVA, Figures 7I and 7J = *p < 0.05, **p < 0.01, ****p < 0.0001; ns, no statistical significance.

Please also see Figures S7H–S7K.

expressed on TAMs elicits their conversion into inflammatory and APC-like macrophages that enhance TCR diversity of tumor-infiltrating T cells. Furthermore, PD-L1-expressing tumor endothelial cells have been demonstrated to directly regulate infiltration, proliferation, and cytotoxicity of CD8⁺ T cells in an antigen-specific manner.^{60,61} While the combination of IL2 with anti-PD-L1 expanded virus-specific CD8⁺ T cells in a lymphocytic choriomeningitis virus (LCMV) infection model,^{62,63} we observed no synergistic expansion of tumor-specific CD8⁺ T cells when anti-PD-L1 was combined with PD1-IL2v. Rather, our data suggest that anti-PD-L1 exerts its beneficial effects not by directly modulating T cells but rather by remodeling TAMs and the tumor vasculature.

Several reports have associated diversity of the TCR repertoire with responsiveness to immunotherapies by extending the spectrum of antigen recognition.^{45,64} Despite increasing TCR diversity, anti-PD-L1 monotherapy did not produce discernable therapeutic benefit in the RT5 model and rather increased the infiltration of CD8⁺ T cells with a terminally exhausted and inactive phenotype. In marked contrast, the combination of anti-PD-L1 with PD1-IL2v elicited clonal expansion of effector memory cytotoxic (and pseudo-exhausted) tumor-antigen specific CD8⁺ T cells that produced an impressive anti-tumor response and survival benefit.

In conclusion, we have demonstrated that delivering the immuno-stimulatory cytokine IL2v to tumor-antigen expressing CD8⁺ T cells in-cis via PD1-IL2v can have potent effects in circumventing inflammatory barriers and rendering checkpoint-inhibitor-insensitive tumors amenable to immune attack, an effect that can be sustained by anti-PD-L1. Notably, the functional effects of anti-PD-L1 do not center upon blocking the PD1 checkpoint on CD8⁺ T cells. Rather, anti-PD-L1 is demonstrably targeting PD-L1 expressed on tumor-infiltrating macrophages and tumor endothelial cells, which reprograms them into pro-inflammatory, antigen-presenting cells that help sustain and enhance the stem-like “resource” and effector CD8⁺ T cell activity triggered by IL2v stimulation conveyed by PD1-IL2v, thereby producing combinatorial therapeutic efficacy.

Collectively, the data obtained in the *de novo* RT5 pancreatic and the glioma transplant tumor models encourage consideration of clinical trials evaluating PD1-IL2v immunocytokine in combination with anti-PD-L1, perhaps initially in anti-PD-1/anti-PD-L1 resistant tumors that are not immune deserts or fully “immune excluded” but rather evidence at least modest infiltration of PD-1⁺ CD8⁺ T cells in the tumor microenvironment.

Limitations of the study

This study reveals the benefit of combining PD1-IL2v and anti-PD-L1 in a model of pancreatic neuroendocrine cancer that is intrinsically resistant to tumor vaccines and ICB. An ostensible limitation of the RT5 model is that tumorigenesis is driven by the SV40 TAG oncoprotein. Despite this caveat, cross-species analyses of PanNETs from the RT2 model and cognate human tumors have revealed broad similarities that substantiate the validity of this mouse model.^{65,66} As illustrated herein, RT5 mice can serve as an instructive model of an immunotherapy-resistant tumor with pre-existing but suppressed stem-like antigen-specific T cells. Although mechanistic aspects were corroborated in a mouse model of glioma, studies in other syngeneic/*de-novo*

mouse models of cancer are needed to extend the generality of the observed effects on TAMs, vasculature, and T cells that result in efficacious anti-tumor immune responses.

STAR★METHODS

Detailed methods are provided in the online version of this paper and include the following:

- **KEY RESOURCES TABLE**
- **RESOURCE AVAILABILITY**
 - Lead contact
 - Materials availability
 - Data and code availability
- **EXPERIMENTAL MODEL AND SUBJECT DETAILS**
 - Mice
 - Cell line
- **METHOD DETAILS**
 - Study design
- **QUANTIFICATION AND STATISTICAL ANALYSIS**
 - Quantification of tissue staining
 - Statistical analysis

SUPPLEMENTAL INFORMATION

Supplemental information can be found online at <https://doi.org/10.1016/j.immuni.2022.12.006>.

ACKNOWLEDGMENTS

The authors thank M. Alexandre-Gaveta, M.W. Peng, S. André-Baflast, and E. Drori for technical support; J. Joyce for the GL261 cell line; R. Combe for assistance in ultrasound imaging; the EPFL BIOP, FCCF, HCF, Gene Expression, and CPG cores; the Agora Center FCF, IVIF, ClF, MPF and AIVC cores. This study was supported by Roche-Glycart, the Ludwig Institute for Cancer Research, and the European Research Council (ERC-AdG-834947).

AUTHOR CONTRIBUTIONS

Conceptualization, S.W., M.T., L.C.D., P.U., C.K., and D.H.; methodology, S.W., M.T., A.C., and K.H.; bioinformatic analysis, N.F, R.M., and A.K.; drafting, S.W. and M.T.; editing, S.W., M.T., K.H., L.C.D., P.U., C.K., A.C., and D.H.; reagents, L.C.D., P.U., and C.K.; supervision, S.W., M.T., and D.H. S.W. and M.T. contributed equally.

DECLARATION OF INTERESTS

D.H. is a Director of Opna Bio; S.W. declares employment and stock with Molecular Partners; and L.C.D., C.K., and P. U. declare employment, patents, and stock with Roche. Roche has filed patent applications 15/943,237 and US20220072103 relevant to this work.

Received: March 4, 2022

Revised: September 29, 2022

Accepted: December 6, 2022

Published: January 10, 2023

REFERENCES

1. Held, W., Siddiqui, I., Schaeuble, K., and Speiser, D.E. (2019). Intratumoral CD8⁺ T cells with stem cell-like properties: implications for cancer immunotherapy. *Sci. Transl. Med.* *11*, eaay6863. <https://doi.org/10.1126/scitranslmed.aay6863>.
2. Siddiqui, I., Schaeuble, K., Chennupati, V., Fuertes Marraco, S.A., Calderon-Copete, S., Pais Ferreira, D., Carmona, S.J., Scarpellino, L.,

- Gfeller, D., Pradervand, S., et al. (2019). Intratumoral Tcf1+PD-1+CD8+ T cells with stem-like properties promote tumor control in response to vaccination and checkpoint blockade immunotherapy. *Immunity* 50, 195–211.e10. <https://doi.org/10.1016/j.immuni.2018.12.021>.
3. Wei, S.C., Duffy, C.R., and Allison, J.P. (2018). Fundamental mechanisms of immune checkpoint blockade therapy. *Cancer Discov.* 8, 1069–1086. <https://doi.org/10.1158/2159-8290.CD-18-0367>.
 4. Schoenfeld, A.J., and Hellmann, M.D. (2020). Acquired resistance to immune checkpoint inhibitors. *Cancer Cell* 37, 443–455. <https://doi.org/10.1016/j.ccell.2020.03.017>.
 5. Boyman, O., and Arenas-Ramirez, N. (2019). Development of a novel class of interleukin-2 immunotherapies for metastatic cancer. *Swiss Med. Wkly.* 149, w14697. <https://doi.org/10.4414/sm.w.2019.14697>.
 6. Ross, S.H., and Cantrell, D.A. (2018). Signaling and function of interleukin-2 in T Lymphocytes. *Annu. Rev. Immunol.* 36, 411–433. <https://doi.org/10.1146/annurev-immunol-042617-053352>.
 7. Malek, T.R., and Castro, I. (2010). Interleukin-2 Receptor Signaling: At the Interface between Tolerance and Immunity. *Immunity* 33, 153–165. <https://doi.org/10.1016/j.immuni.2010.08.004>.
 8. Mortara, L., Balza, E., Bruno, A., Poggi, A., Orecchia, P., and Carnemolla, B. (2018). Anti-cancer therapies employing IL-2 cytokine tumor targeting: contribution of innate, adaptive and immunosuppressive cells in the anti-tumor efficacy. *Front. Immunol.* 9, 2905. <https://doi.org/10.3389/fimmu.2018.02905>.
 9. Neri, D., and Sondel, P.M. (2016). Immunocytokines for cancer treatment: past, present and future. *Curr. Opin. Immunol.* 40, 96–102. <https://doi.org/10.1016/j.coi.2016.03.006>.
 10. Chen, X., Ai, X., Wu, C., Wang, H., Zeng, G., Yang, P., and Liu, G. (2018). A novel human IL-2 mutein with minimal systemic toxicity exerts greater antitumor efficacy than wild-type IL-2. *Cell Death Dis.* 9, 989. <https://doi.org/10.1038/s41419-018-1047-2>.
 11. Klein, C., Waldhauer, I., Nicolini, V., Dunn, C., Freimoser-Grundschober, A., Danny, G., Boerman, O., Nayak, T., Herter, S., Van Puijenbroek, E., et al. (2013). Novel tumor-targeted, engineered IL-2 variant (IL2v)-based immunocytokines for immunotherapy of cancer. *Blood* 122, 2278. <https://doi.org/10.1182/blood.V122.21.2278.2278>.
 12. Klein, C., Waldhauer, I., Nicolini, V.G., Freimoser-Grundschober, A., Nayak, T., Vugts, D.J., Dunn, C., Boliijn, M., Benz, J., Stihle, M., et al. (2017). Cergutuzumab amunaleukin (CEA-IL2v), a CEA-targeted IL-2 variant-based immunocytokine for combination cancer immunotherapy: Overcoming limitations of aldesleukin and conventional IL-2-based immunocytokines. *Oncolimmunology* 6, e1277306. <https://doi.org/10.1080/2162402X.2016.1277306>.
 13. Levin, A.M., Bates, D.L., Ring, A.M., Krieg, C., Lin, J.T., Su, L., Moraga, I., Raeber, M.E., Bowman, G.R., Novick, P., et al. (2012). Exploiting a natural conformational switch to engineer an interleukin-2 'superkine'. *Nature* 484, 529–533. <https://doi.org/10.1038/nature10975>.
 14. Spolski, R., Li, P., and Leonard, W.J. (2018). Biology and regulation of IL-2: from molecular mechanisms to human therapy. *Nat. Rev. Immunol.* 18, 648–659. <https://doi.org/10.1038/s41577-018-0046-y>.
 15. Sun, Z., Ren, Z., Yang, K., Liu, Z., Cao, S., Deng, S., Xu, L., Liang, Y., Guo, J., Bian, Y., et al. (2019). A next-generation tumor-targeting IL-2 preferentially promotes tumor-infiltrating CD8+ T-cell response and effective tumor control. *Nat. Commun.* 10, 3874. <https://doi.org/10.1038/s41467-019-11782-w>.
 16. Codarri Deak, L., Nicolini, V., Hashimoto, M., Karagianni, M., Schwalie, P.C., Lauener, L., Varypataki, E.M., Richard, M., Bommer, E., Sam, J., et al. (2022). PD-1-cis IL-2R agonism yields better effectors from stem-like CD8+ T cells. *Nature* 610, 161–172. <https://doi.org/10.1038/s41586-022-05192-0>.
 17. Di Pilato, M., Kfuri-Rubens, R., Pruessmann, J.N., Ozga, A.J., Messemaker, M., Cadilha, B.L., Sivakumar, R., Cianciaruso, C., Warner, R.D., Marangoni, F., et al. (2021). CXCR6 positions cytotoxic T cells to receive critical survival signals in the tumor microenvironment. *Cell* 184, 4512–4530.e22. <https://doi.org/10.1016/j.cell.2021.07.015>.
 18. Hudson, W.H., Gensheimer, J., Hashimoto, M., Wieland, A., Valanparambil, R.M., Li, P., Lin, J.-X., Konieczny, B.T., Im, S.J., Freeman, G.J., et al. (2019). Proliferating transitory T cells with an effector-like transcriptional signature emerge from PD-1+ stem-like CD8+ T cells during chronic infection. *Immunity* 51, 1043–1058.e4. <https://doi.org/10.1016/j.immuni.2019.11.002>.
 19. Mo, F., Yu, Z., Li, P., Oh, J., Spolski, R., Zhao, L., Glassman, C.R., Yamamoto, T.N., Chen, Y., Golebiowski, F.M., et al. (2021). An engineered IL-2 partial agonist promotes CD8+ T cell stemness. *Nature* 597, 544–548. <https://doi.org/10.1038/s41586-021-03861-0>.
 20. Sade-Feldman, M., Yizhak, K., Bjorgaard, S.L., Ray, J.P., de Boer, C.G., Jenkins, R.W., Lieb, D.J., Chen, J.H., Frederick, D.T., Barzily-Rokni, M., et al. (2018). Defining T cell states associated with response to checkpoint immunotherapy in melanoma. *Cell* 175, 998–1013.e20. <https://doi.org/10.1016/j.cell.2018.10.038>.
 21. Adams, T.E., Alpert, S., and Hanahan, D. (1987). Non-tolerance and auto-antibodies to a transgenic self antigen expressed in pancreatic beta cells. *Nature* 325, 223–228. <https://doi.org/10.1038/325223a0>.
 22. Skowronski, J., Jolicoeur, C., Alpert, S., and Hanahan, D. (1990). Determinants of the B-cell response against a transgenic autoantigen. *Proc. Natl. Acad. Sci. USA.* 87, 7487–7491. <https://doi.org/10.1073/pnas.87.19.7487>.
 23. Ganss, R., and Hanahan, D. (1998). Tumor microenvironment can restrict the effectiveness of activated antitumor lymphocytes. *Cancer Res.* 58, 4673–4681.
 24. Onrust, S.V., Hartl, P.M., Rosen, S.D., and Hanahan, D. (1996). Modulation of L-selectin ligand expression during an immune response accompanying tumorigenesis in transgenic mice. *J. Clin. Invest.* 97, 54–64. <https://doi.org/10.1172/JCI118406>.
 25. Garbi, N., Arnold, B., Gordon, S., Hämmerling, G.J., and Ganss, R. (2004). CpG motifs as proinflammatory factors render autochthonous tumors permissive for infiltration and destruction. *J. Immunol.* 172, 5861–5869. <https://doi.org/10.4049/jimmunol.172.10.5861>.
 26. Johansson-Percival, A., He, B., Li, Z.-J., Kjellén, A., Russell, K., Li, J., Larma, I., and Ganss, R. (2017). De novo induction of intratumoral lymphoid structures and vessel normalization enhances immunotherapy in resistant tumors. *Nat. Immunol.* 18, 1207–1217. <https://doi.org/10.1038/ni.3836>.
 27. Oh, D.Y., Kwek, S.S., Raju, S.S., Li, T., McCarthy, E., Chow, E., Aran, D., Ilano, A., Pai, C.-C.S., Rancan, C., et al. (2020). Intratumoral CD4+ T cells mediate anti-tumor cytotoxicity in human bladder cancer. *Cell* 181, 1612–1625.e13. <https://doi.org/10.1016/j.cell.2020.05.017>.
 28. Zou, W., Wolchok, J.D., and Chen, L. (2016). PD-L1 (B7-H1) and PD-1 pathway blockade for cancer therapy: mechanisms, response biomarkers, and combinations. *Sci. Transl. Med.* 8, 328rv4. <https://doi.org/10.1126/scitranslmed.aad7118>.
 29. Spranger, S., Spaapen, R.M., Zha, Y., Williams, J., Meng, Y., Ha, T.T., and Gajewski, T.F. (2013). Up-regulation of PD-L1, IDO, and tregs in the melanoma tumor microenvironment is driven by CD8+ T cells. *Sci. Transl. Med.* 5, 200ra116. <https://doi.org/10.1126/scitranslmed.3006504>.
 30. Taube, J.M., Anders, R.A., Young, G.D., Xu, H., Sharma, R., McMiller, T.L., Chen, S., Klein, A.P., Pardoll, D.M., Topalian, S.L., and Chen, L. (2012). Colocalization of inflammatory response with B7-H1 expression in human melanocytic lesions supports an adaptive resistance mechanism of immune escape. *Sci. Transl. Med.* 4, 127ra37. <https://doi.org/10.1126/scitranslmed.3003689>.
 31. Andreatta, M., Corria-Osorio, J., Müller, S., Cubas, R., Coukos, G., and Carmona, S.J. (2021). Interpretation of T cell states from single-cell transcriptomics data using reference atlases. *Nat. Commun.* 12, 2965. <https://doi.org/10.1038/s41467-021-23324-4>.
 32. Mylin, L.M., Bonneau, R.H., Lippolis, J.D., and Tevethia, S.S. (1995). Hierarchy among multiple H-2b-restricted cytotoxic T-lymphocyte epitopes within simian virus 40 T antigen. *J. Virol.* 69, 6665–6677. <https://doi.org/10.1128/jvi.69.11.6665-6677.1995>.

33. Staveley-O'Carroll, K., Schell, T.D., Jimenez, M., Mylin, L.M., Tevethia, M.J., Schoenberger, S.P., and Tevethia, S.S. (2003). In vivo ligation of CD40 enhances priming against the endogenous tumor antigen and promotes CD8⁺ T cell effector function in SV40 T antigen transgenic mice. *J. Immunol.* *171*, 697–707. <https://doi.org/10.4049/jimmunol.171.2.697>.
34. Textor, A., Schmidt, K., Kloetzel, P.-M., Weißbrich, B., Perez, C., Charo, J., Anders, K., Sidney, J., Sette, A., Schumacher, T.N.M., et al. (2016). Preventing tumor escape by targeting a post-proteasomal trimming independent epitope. *J. Exp. Med.* *213*, 2333–2348. <https://doi.org/10.1084/jem.20160636>.
35. DeNardo, D.G., and Ruffell, B. (2019). Macrophages as regulators of tumour immunity and immunotherapy. *Nat. Rev. Immunol.* *19*, 369–382. <https://doi.org/10.1038/s41577-019-0127-6>.
36. Xiong, H., Mittman, S., Rodriguez, R., Moskalenko, M., Pacheco-Sanchez, P., Yang, Y., Nickles, D., and Cubas, R. (2019). Anti-PD-L1 treatment results in functional remodeling of the macrophage compartment. *Cancer Res.* *79*, 1493–1506. <https://doi.org/10.1158/0008-5472.CAN-18-3208>.
37. Molgora, M., Esaulova, E., Vermi, W., Hou, J., Chen, Y., Luo, J., Brioschi, S., Bugatti, M., Omodei, A.S., Ricci, B., et al. (2020). TREM2 modulation remodels the tumor myeloid landscape enhancing anti-PD-1 immunotherapy. *Cell* *182*, 886–900.e17. <https://doi.org/10.1016/j.cell.2020.07.013>.
38. Browaeys, R., Saelens, W., and Saeys, Y. (2020). NicheNet: modeling intercellular communication by linking ligands to target genes. *Nat. Methods* *17*, 159–162. <https://doi.org/10.1038/s41592-019-0667-5>.
39. Chryplewicz, A., Scotton, J., Tichet, M., Zomer, A., Shchors, K., Joyce, J.A., Homicsko, K., and Hanahan, D. (2022). Cancer cell autophagy, reprogrammed macrophages, and remodeled vasculature in glioblastoma triggers tumor immunity. *Cancer Cell* *40*, 1111–1127.e9. <https://doi.org/10.1016/j.ccell.2022.08.014>.
40. Szatmári, T., Lumniczky, K., Désaknai, S., Trajcevski, S., Hídvégi, E.J., Hamada, H., and Sáfrány, G. (2006). Detailed characterization of the mouse glioma 261 tumor model for experimental glioblastoma therapy. *Cancer Sci.* *97*, 546–553. <https://doi.org/10.1111/j.1349-7006.2006.00208.x>.
41. Ren, Z., Zhang, A., Sun, Z., Liang, Y., Ye, J., Qiao, J., Li, B., and Fu, Y.-X. (2022). Selective delivery of low-affinity IL-2 to PD-1⁺ T cells rejuvenates antitumor immunity with reduced toxicity. *J. Clin. Invest.* *132*, e153604. <https://doi.org/10.1172/JCI153604>.
42. Willimsky, G., and Blankenstein, T. (2005). Sporadic immunogenic tumours avoid destruction by inducing T-cell tolerance. *Nature* *437*, 141–146. <https://doi.org/10.1038/nature03954>.
43. Willimsky, G., Czéh, M., Loddenkemper, C., Gellermann, J., Schmidt, K., Wust, P., Stein, H., and Blankenstein, T. (2008). Immunogenicity of premalignant lesions is the primary cause of general cytotoxic T lymphocyte unresponsiveness. *J. Exp. Med.* *205*, 1687–1700. <https://doi.org/10.1084/jem.20072016>.
44. Miller, B.C., Sen, D.R., Al Aboosy, R., Bi, K., Virkud, Y.V., LaFleur, M.W., Yates, K.B., Lako, A., Felt, K., Naik, G.S., et al. (2019). Subsets of exhausted CD8⁺ T cells differentially mediate tumor control and respond to checkpoint blockade. *Nat. Immunol.* *20*, 326–336. <https://doi.org/10.1038/s41590-019-0312-6>.
45. Burger, M.L., Cruz, A.M., Crossland, G.E., Gaglia, G., Ritch, C.C., Blatt, S.E., Bhutkar, A., Canner, D., Kienka, T., Tavana, S.Z., et al. (2021). Antigen dominance hierarchies shape TCF1⁺ progenitor CD8⁺ T cell phenotypes in tumors. *Cell* *184*, 4996–5014.e26. <https://doi.org/10.1016/j.cell.2021.08.020>.
46. Jansen, C.S., Prokhnivska, N., Master, V.A., Sanda, M.G., Carlisle, J.W., Bilen, M.A., Cardenas, M., Wilkinson, S., Lake, R., Sowalsky, A.G., et al. (2019). An intra-tumoral niche maintains and differentiates stem-like CD8⁺ T cells. *Nature* *576*, 465–470. <https://doi.org/10.1038/s41586-019-1836-5>.
47. Krishna, S., Lowery, F.J., Copeland, A.R., Bahadiroglu, E., Mukherjee, R., Jia, L., Anibal, J.T., Sachs, A., Adebola, S.O., Gurusamy, D., et al. (2020). Stem-like CD8⁺ T cells mediate response of adoptive cell immunotherapy against human cancer. *Science* *370*, 1328–1334. <https://doi.org/10.1126/science.abb9847>.
48. Spitzer, M.H., Carmi, Y., Reticker-Flynn, N.E., Kwek, S.S., Madhiredy, D., Martins, M.M., Gherardini, P.F., Prestwood, T.R., Chabon, J., Bendall, S.C., et al. (2017). Systemic immunity is required for effective cancer immunotherapy. *Cell* *168*, 487–502.e15. <https://doi.org/10.1016/j.cell.2016.12.022>.
49. Motz, G.T., Santoro, S.P., Wang, L.-P., Garrabrant, T., Lastra, R.R., Hagemann, I.S., Lal, P., Feldman, M.D., Benencia, F., and Coukos, G. (2014). Tumor endothelium FasL establishes a selective immune barrier promoting tolerance in tumors. *Nat. Med.* *20*, 607–615. <https://doi.org/10.1038/nm.3541>.
50. Hamzah, J., Jugold, M., Kiessling, F., Rigby, P., Manzur, M., Marti, H.H., Rabie, T., Kaden, S., Gröne, H.J., Hämmerling, G.J., et al. (2008). Vascular normalization in Rgs5-deficient tumours promotes immune destruction. *Nature* *453*, 410–414. <https://doi.org/10.1038/nature06868>.
51. Allen, E., Jabouille, A., Rivera, L.B., Lodewijckx, I., Missiaen, R., Steri, V., Feyen, K., Tawney, J., Hanahan, D., Michael, I.P., and Bergers, G. (2017). Combined antiangiogenic and anti-PD-L1 therapy stimulates tumor immunity through HEV formation. *Sci. Transl. Med.* *9*, eaak9679. <https://doi.org/10.1126/scitranslmed.aak9679>.
52. Asrir, A., Tardiveau, C., Coudert, J., Laffont, R., Blanchard, L., Bellard, E., Veerman, K., Bettini, S., Lafouresse, F., Vina, E., et al. (2022). Tumor-associated high endothelial venules mediate lymphocyte entry into tumors and predict response to PD-1 plus CTLA-4 combination immunotherapy. *Cancer Cell* *40*, 318–334.e9. <https://doi.org/10.1016/j.ccell.2022.01.002>.
53. Held, W., Luther, S.A., and Petrova, T.V. (2022). Stem-cell-like T cells have a specific entry gate to the tumor. *Cancer Cell* *40*, 243–245. <https://doi.org/10.1016/j.ccell.2022.02.004>.
54. Hua, Y., Vella, G., Rambow, F., Allen, E., Antoranz Martinez, A., Duhamel, M., Takeda, A., Jalkanen, S., Junius, S., Smeets, A., et al. (2022). Cancer immunotherapies transition endothelial cells into HEVs that generate TCF1⁺ T lymphocyte niches through a feed-forward loop. *Cancer Cell* *51*, 605–618. <https://doi.org/10.1016/j.ccell.2022.11.002>.
55. Klug, F., Prakash, H., Huber, P.E., Seibel, T., Bender, N., Halama, N., Pfirschke, C., Voss, R.H., Timke, C., Umansky, L., et al. (2013). Low-dose irradiation programs macrophage differentiation to an iNOS⁺/M1 phenotype that orchestrates effective T cell immunotherapy. *Cancer Cell* *24*, 589–602. <https://doi.org/10.1016/j.ccr.2013.09.014>.
56. Mayoux, M., Roller, A., Pulko, V., Sammiceli, S., Chen, S., Sum, E., Jost, C., Fransen, M.F., Buser, R.B., Kowanetz, M., et al. (2020). Dendritic cells dictate responses to PD-L1 blockade cancer immunotherapy. *Sci. Transl. Med.* *12*, eaav7431. <https://doi.org/10.1126/scitranslmed.aav7431>.
57. Philip, M., and Schietinger, A. (2021). CD8⁺ T cell differentiation and dysfunction in cancer. *Nat. Rev. Immunol.* *22*, 209–223. <https://doi.org/10.1038/s41577-021-00574-3>.
58. Wang, Y., Liu, S., Yang, Z., Algazi, A.P., Lomeli, S.H., Wang, Y., Othus, M., Hong, A., Wang, X., Randolph, C.E., et al. (2021). Anti-PD-1/L1 lead-in before MAPK inhibitor combination maximizes antitumor immunity and efficacy. *Cancer Cell* *39*, 1375–1387.e6. <https://doi.org/10.1016/j.ccell.2021.07.023>.
59. Zhang, Y., Chen, H., Mo, H., Hu, X., Gao, R., Zhao, Y., Liu, B., Niu, L., Sun, X., Yu, X., et al. (2021). Single-cell analyses reveal key immune cell subsets associated with response to PD-L1 blockade in triple-negative breast cancer. *Cancer Cell* *39*, 1578–1593.e8. <https://doi.org/10.1016/j.ccell.2021.09.010>.
60. Rodig, N., Ryan, T., Allen, J.A., Pang, H., Grabie, N., Chernova, T., Greenfield, E.A., Liang, S.C., Sharpe, A.H., Lichtman, A.H., and Freeman, G.J. (2003). Endothelial expression of PD-L1 and PD-L2 down-regulates CD8⁺ T cell activation and cytotoxicity. *Eur. J. Immunol.* *33*, 3117–3126. <https://doi.org/10.1002/eji.200324270>.
61. Taguchi, K., Onoe, T., Yoshida, T., Yamashita, Y., Tanaka, Y., and Ohdan, H. (2020). Tumor endothelial cell-mediated antigen-specific T-cell

- suppression via the PD-1/PD-L1 pathway. *Mol. Cancer Res.* **18**, 1427–1440. <https://doi.org/10.1158/1541-7786.MCR-19-0897>.
62. West, E.E., Jin, H.-T., Rasheed, A.-U., Penaloza-MacMaster, P., Ha, S.-J., Tan, W.G., Youngblood, B., Freeman, G.J., Smith, K.A., and Ahmed, R. (2013). PD-L1 blockade synergizes with IL-2 therapy in reinvigorating exhausted T cells. *J. Clin. Invest.* **123**, 2604–2615. <https://doi.org/10.1172/JCI67008>.
 63. Hashimoto, M., Araki, K., Cardenas, M.A., Li, P., Jadhav, R.R., Kissick, H.T., Hudson, W.H., McGuire, D.J., Obeng, R.C., Wieland, A., et al. (2022). PD-1 combination therapy with IL-2 modifies CD8+ T cell exhaustion program. *Nature* **610**, 173–181. <https://doi.org/10.1038/s41586-022-05257-0>.
 64. Hosoi, A., Takeda, K., Nagaoka, K., Iino, T., Matsushita, H., Ueha, S., Aoki, S., Matsushima, K., Kubo, M., Morikawa, T., et al. (2018). Increased diversity with reduced “diversity evenness” of tumor infiltrating T-cells for the successful cancer immunotherapy. *Sci. Rep.* **8**, 1058. <https://doi.org/10.1038/s41598-018-19548-y>.
 65. Sadanandam, A., Wullschleger, S., Lyssiotis, C.A., Grötzing, C., Barbi, S., Bersani, S., Körner, J., Wafy, I., Mafficini, A., Lawlor, R.T., et al. (2015). A cross-species analysis in pancreatic neuroendocrine tumors reveals molecular subtypes with distinctive clinical, metastatic, developmental, and metabolic characteristics. *Cancer Discov.* **5**, 1296–1313. <https://doi.org/10.1158/2159-8290.CD-15-0068>.
 66. Saghafinia, S., Homicsko, K., Di Domenico, A., Wullschleger, S., Perren, A., Marinoni, I., Ciriello, G., Michael, I.P., and Hanahan, D. (2021). Cancer cells retrace a stepwise differentiation program during malignant progression. *Cancer Discov.* **11**, 2638–2657. <https://doi.org/10.1158/2159-8290.CD-20-1637>.
 67. Bankhead, P., QuPath, et al. (2017). Open source software for digital pathology image analysis. *Scientific Reports.* <https://doi.org/10.1038/s41598-017-17204-5>.
 68. Shugay, M., Bagaev, D.V., Turchaninova, M.A., Bolotin, D.A., Britanova, O.V., Putintseva, E.V., Pogorelyy, M.V., Nazarov, V.I., Zvyagin, I.V., Kirgizova, V.I., et al. (2015). VDJtools: unifying post-analysis of T cell receptor repertoires. *PLoS Comput. Biol.* **11**, e1004503. <https://doi.org/10.1371/journal.pcbi.1004503>.
 69. Nazarov, V., Bot, I., and Rumynskiy, E. (2020). Immunomind/Immunarch: 0.6.5: Basic Single-Cell Support. <https://doi.org/10.5281/ZENODO.3367200>.
 70. Zheng, G.X.Y., Terry, J.M., Belgrader, P., Ryvkin, P., Bent, Z.W., Wilson, R., Ziraldo, S.B., Wheeler, T.D., McDermott, G.P., Zhu, J., et al. (2017). Massively parallel digital transcriptional profiling of single cells. *Nat. Commun.* **8**, 14049. <https://doi.org/10.1038/ncomms14049>.
 71. Bolotin, D.A., Poslavsky, S., Mitrophanov, I., Shugay, M., Mamedov, I.Z., Putintseva, E.V., and Chudakov, D.M. (2015). MiXCR: software for comprehensive adaptive immunity profiling. *Nat. Methods* **12**, 380–381. <https://doi.org/10.1038/nmeth.3364>.
 72. Bagaev, D.V., Vroomans, R.M.A., Samir, J., Stervbo, U., Rius, C., Dolton, G., Greenshields-Watson, A., Attaf, M., Egorov, E.S., Zvyagin, I.V., et al. (2020). VDJdb in 2019: database extension, new analysis infrastructure and a T-cell receptor motif compendium. *Nucleic Acids Res.* **48**, D1057–D1062. <https://doi.org/10.1093/nar/gkz874>.

STAR★METHODS

KEY RESOURCES TABLE

| REAGENT or RESOURCE | SOURCE | IDENTIFIER |
|---|------------------------|--------------------------------------|
| Antibodies | | |
| PD1-IL2v (muPD1-IL2v) | Roche | N/A |
| anti-PDL-1 (anti-muPD-L1) | Roche | N/A |
| anti-PD-1 (anti-muPD-1) | Roche | N/A |
| IgG-IL2v (DP47-muIL2v) | Roche | N/A |
| InVivoMAb anti-mouse CD8a (clone 2.43) | BioXCell | Cat #: BE0061; RRID: AB_1125541 |
| InVivoMAb anti-mouse CD4 (clone GK1.5) | BioXCell | Cat #: BE0003-1; RRID: AB_1107636 |
| InVivoPlus anti-mouse IFNg (clone XMG1.2) | BioXCell | Cat #: BP0055; RRID: AB_1107694 |
| Purified anti-mouse CD16/32 | Biolegend | Cat#: 101302; RRID: AB_312801 |
| SV40 TAG multimer (APC-MHC-H2Kb-VVYDFLKC) | University of Lausanne | N/A |
| CD4 Brilliant Violet 510 (clone RM4-5) | Biolegend | Cat #: 100,559; RRID: AB_2562608 |
| CD4 PE-Cyanine7 (clone RM4-5) | Biolegend | Cat #: 100,528; RRID: AB_312729 |
| CD4 PE (clone GK1.5) | Biolegend | Cat #: 100,408; RRID: AB_312693 |
| CD8a FITC (clone 53-6.7) | Biolegend | Cat #: 100,706; RRID: AB_312745 |
| CD8a BB515 (clone 53-6.7) | BD Biosciences | Cat #: 564,422; RRID: AB_2738801 |
| CD8a PE-Cyanine7 (clone 53-6.7) | Biolegend | Cat #: 100,722; RRID: AB_312761 |
| CD8a Pacific Orange (clone 5H10) | Invitrogen | Cat #: MCD0830; RRID: AB_10376311 |
| CD8a Alexa Fluor 647 (clone 53-6.7) | Biolegend | Cat #: 100,724; RRID: AB_389326 |
| PD-1 PE-Cyanine7 (clone RMP1-30) | Biolegend | Cat #: 109,110; RRID: AB_572017 |
| PD-1 PE (clone RMP1-30) | eBioscience | Cat #: 12-9981-82; RRID: AB_466290 |
| CD127 (IL-7Ra) Brilliant Violet 650 (clone A7R34) | Biolegend | Cat #: 135,043; RRID: AB_2629681 |
| FoxP3 PE (clone FJK-16s) | Invitrogen | Cat #: 12-5773-82; RRID: AB_465936 |
| CD218a (IL-18Ra) APC (clone B3TUNYA) | eBioscience | Cat #: 17-5183-82; RRID: AB_2744708 |
| TCF-7/TCF-1 Brilliant Violet 421 (clone FJK-16s) | BD Biosciences | Cat #: 566,692; RRID: AB_2869822 |
| TCF-7/TCF-1 PE (clone FJK-16s) | BD Biosciences | Cat#: 564217; RRID: AB_2687845 |
| CD3e FITC (clone 145-2C11) | eBioscience | Cat #: 11-0031-82; RRID: AB_464882 |
| CD3e PerCP-Cyanine5.5 (clone 145-2C11) | eBioscience | Cat #: 45-0031-82; RRID: AB_1107000 |
| CD3e PE-Cyanine5 (clone 145-2C11) | eBioscience | Cat #: 15-0031-82; RRID: AB_468690 |
| Tim3 PE (clone B8.2C12) | Biolegend | Cat #: 134,004; RRID: AB_1626177 |
| Tim3 PE/Dazzle 594 (clone B8.2C12) | Biolegend | Cat #: 134,014; RRID: AB_2632738 |
| CD11b PerCP-Cyanine5.5 (clone M1/70) | eBioscience | Cat #: 45-0112-82; RRID: AB_953558 |
| CD11b Biotin (clone M1/70) | eBioscience | Cat #: 13-0112-82; RRID: AB_466359 |
| CD11b Pacific Blue (M1/70) | Biolegend | Cat #: 101,224; RRID: AB_755986 |
| CD11b PE-Cyanine7 (clone M1/70) | eBioscience | Cat #: 25-0112-82; RRID: AB_469588 |
| B220 (CD45R) PerCP-Cyanine5.5 (clone RA3-6B2) | eBioscience | Cat #: 45-0452-82; RRID: AB_1107006 |
| CD45 APC/Cyanine7 (clone 30-F11) | Biolegend | Cat #: 103,116; RRID: AB_312981 |
| CD45 Biotin (clone 30-F11) | eBioscience | Cat #: 13-0451-82; RRID: AB_466446 |
| CD45 Pacific Orange (clone 30-F11) | Invitrogen | Cat #: MCD4530; RRID: AB_2539700 |
| CD45 BUV395 (clone 30-F11) | BD Biosciences | Cat #: 564,279; RRID: AB_2651134 |
| CD44 APC-eFluor 780 (clone IM7) | eBioscience | Cat #: 47-0441-82; RRID: AB_1272244 |
| CD62L FITC (clone MEL-14) | Biolegend | Cat#: 104406; RRID: AB_313093 |
| TNFa FITC (cloneMP6-XT22) | eBioscience | Cat #: 11-7321-82; RRID: AB_465418 |
| Granzyme B (GZMB) PE (clone NGZB) | eBioscience | Cat #: 12-8898-82; RRID: AB_10870787 |
| IFNg APC (clone XMG1.2) | Biolegend | Cat #: 505,810; RRID: AB_315403 |
| F4/80 PE (clone BM8) | eBioscience | Cat#: 12-4801-82; RRID: AB_465923 |

(Continued on next page)

Continued

| REAGENT or RESOURCE | SOURCE | IDENTIFIER |
|---|---------------------|--------------------------------------|
| Arginase 1 Alexa Fluor 488 (clone A1exF5) | eBioscience | Cat#: 53-3697-82; RRID: AB_2734831 |
| Ly-6C PerCP-Cyanine5.5 (clone HK1.4) | eBioscience | Cat#: 45-5932-82; RRID: AB_2723343 |
| Ly-6G Pacific Blue (clone 1A8) | Biolegend | Cat#: 127612; RRID: AB_2251161 |
| CD206 (Mrc1) Alexa Fluor 647 (clone C068C2) | Biolegend | Cat#: 141712; RRID: AB_10900420 |
| II-10 APC/Cyanine7 (clone JES5-16E3) | Biolegend | Cat#: 505036; RRID: AB_2566331 |
| Ki67 PE-Cyanine7 (clone SolA15) | eBioscience | Cat #: 25-5698-82; RRID: AB_11220070 |
| CD274 (B7-H1, PD-L1) PE (clone MIH5) | Invitrogen | Cat #: 12-5982-82; RRID: AB_466089 |
| I-A/I-E (MHCII) FITC (clone M5/114.15.2) | Biolegend | Cat#: 107606; RRID: AB_313321 |
| CD31 FITC (clone MEC 13.3) | BD Biosciences | Cat#: 553372; RRID: AB_394818 |
| CD31 PE (clone MEC 13.3) | BD Biosciences | Cat#: 553373; RRID: AB_394819 |
| T-Antigen (TAG) | In house production | N/A |
| High Endothelial Venule Marker (MECA-79), Alexa Fluor 488 | eBioscience | Cat #: 53-6036-82; RRID: AB_10804391 |
| Alexa Fluor 647 donkey Anti-Rabbit IgG H&L | Abcam | Cat#: ab150075; RRID: AB_2752244 |

Chemicals, Peptides, and Recombinant Proteins

| | | |
|--|----------------|-------------------------|
| FoxP3 staining kit | Invitrogen | Cat#: 00-5523-00 |
| CFSE 5(6)-CFDA | Invitrogen | Cat#: C1157 |
| Dynabeads Mouse T-Activator CD3/CD28 | Gibco | Cat#: 11452D |
| Streptavidin Brilliant Violet 421 conjugate | Biolegend | Cat#: 405226 |
| Streptavidin Pacific Orange conjugate | Invitrogen | Cat#: S32365 |
| DAPI | Roche | Cat#: 10236276001 |
| LIVE/DEAD Fixable Violet Dead Cell Stain Kit | Invitrogen | Cat#: L34964 |
| LIVE/DEAD Fixable Red Dead Cell Stain Kit | Invitrogen | Cat#: L23102 |
| PrimeScript RT Master Mix | Takara | Cat#: RR036A |
| miRNeasy Micro Kit | Qiagen | Cat#: 217084 |
| QuantiNova SYBR Green PCR Kit | Qiagen | Cat#: 208052 |
| Fluorescence Mounting Medium | DAKO | Cat#: S302380 |
| PharmLyse buffer | BD Biosciences | Cat#: 555899 |
| Percoll | Sigma-Adrich | Cat#: Cytiva 17-0891-01 |
| Dispase II (neutral protease, grade II) | Roche | Cat#: 04942078001 |
| DNase I recombinant | Roche | Cat#: 04716728001 |
| Collagenase A | Roche | Cat#: 10103578001 |

Critical Commercial Assays

| | | |
|--|-----------------------|-------------------|
| EasySep Mouse CD11b Positive Selection Kit II | StemCell Technologies | Cat#: 18970 |
| EasySep Mouse CD8 ⁺ T cell Isolation Kit | StemCell Technologies | Cat#: 19853 |
| CD31 Micro-Beads, mouse | Miltenyi Biotec | Cat#: 130-097-418 |
| 10X Chromium 5' v2 kit dual index | 10x genomics | Cat #: PN-1000263 |
| 10X Chromium Single Cell mouse TCR amplification kit | 10x genomics | Cat #: PN-1000254 |

Deposited Data

| | | |
|--------------------------------|------------|-----------|
| scRNAseq and scTCRseq datasets | This paper | GSE197854 |
|--------------------------------|------------|-----------|

Experimental Models: Cell Lines

| | | |
|-------|------------------------|----------------|
| GL261 | provided by J.A. Joyce | RRID:CVCL_Y003 |
|-------|------------------------|----------------|

Experimental Models: Organisms/Strains

| | | |
|---|---------------|------------------|
| Mouse: RIP1-Tag5 (RT5): C57BL6.Tg(RIP1-Tag)5Dh | In house | This paper |
| Mouse: C57BL/6J (JAX Mice Strain) | Charles River | Strain Code: 632 |

Oligonucleotides

Primers: see [Table S4](#)

(Continued on next page)

Continued

| REAGENT or RESOURCE | SOURCE | IDENTIFIER |
|---|--------------------------------|---|
| Software and Algorithms | | |
| QuPath (version 0.2.3) | Bankhead et al. ⁶⁷ | https://qupath.github.io |
| FlowJo (version 10.7.2) | BD | https://www.flowjo.com |
| GraphPad Prism (version 9.4.1) | Dotmatics | https://www.graphpad.com |
| Cell Ranger (v5.0.1) | 10x genomics | https://support.10xgenomics.com/ |
| Seurat (v4.0.4) | | https://satijalab.org/seurat/ |
| ProjecTILs (v1.0.0) | Andreatta et al. ³¹ | N/A |
| muscat (v1.4.0) | N/A | N/A |
| clusterProfiler (v3.18.1) | N/A | N/A |
| VDJTools (version 1.2.1) | Shugay et al. ⁶⁸ | N/A |
| immunarch library (version 0.6.4) | Nazarov et al. ⁶⁹ | N/A |
| Mouse VDJDB | | https://vdjdb.cdr3.net |
| NicheNet (package nichenetr, version 1.0.0) | Browaeys et al. ³⁸ | N/A |
| R (version 4.0) | The R Foundation | https://www.r-project.org/ |

RESOURCE AVAILABILITY

Lead contact

Further information and requests for resources should be directed to and will be fulfilled by the lead contact, Douglas Hanahan (douglas.hanahan@epfl.ch).

Materials availability

This study did not generate new, unique reagents.

Data and code availability

- Single-cell RNA-seq and Single-cell TCR-seq data have been deposited at GEO and are publicly available as of the date of publication. The accession number is listed in the [key resources table](#).
- This paper does not report original code.
- Any additional information required to reanalyze the data reported in this paper is available from the [lead contact](#) upon request.

EXPERIMENTAL MODEL AND SUBJECT DETAILS

Mice

The RT5 transgenic mouse model of PanNET was established by D.H.,²⁴ and bred in our facility (EPFL's CpG core facility). RT5 mice are on a C57BL6/N background (Charles River); only male littermates were used as the females in this model have a more variable pattern of tumorigenesis that would require excessive numbers of female mice to be utilized to assemble statistically significant cohort. Littermate mice were randomly assigned to experimental groups as described in the methods details section.

C57BL/6J mice (both males and females) were purchased from Janvier. Six to ten-week-old mice were used for intracranial GL261 cell injection. Littermate mice of the same sex were randomly assigned to experimental groups.

All mouse strains were housed in pathogen-free facilities in Lausanne (the AIVC animal care facility in the Agora Cancer Research Center and EPFL's CpG core facility) in IVC Cages, 5 animals per cage of 500 cm² with water and food *ad libitum* and enrichment. All animal studies were performed in accordance with licenses VD3133, VD3475 and VD3183 approved by the Veterinary Authorities of the Canton Vaud.

Cell line

The GL261 glioma cell line⁴⁰ (male) was provided by Professor Johanna Joyce (UNIL/Ludwig Institute, Lausanne, Switzerland). The GL261 cell line was grown in DMEM supplemented with 10% fetal bovine serum (FBS), and penicillin/streptomycin. Cells were cultured in a 37°C incubator with 5% CO₂ and routinely monitored for mycoplasma contamination.

METHOD DETAILS

Study design

This study was designed to assess the potential anti-tumoral impact of the PD1-IL2v immunocytokine with and without the addition of anti-PD-L1 in mouse cancer models. We evaluated the efficacy of combinatorial treatments principally in a transgenic mouse model

of neuroendocrine tumor (RT5), supplemented by an orthotopic cell transplant (GL261) mouse model of glioblastoma. We focused on their effects on tumor and immune system phenotypes. All animal studies were performed in accordance with experimental licenses approved by the Veterinary Authorities of the Canton Vaud. The design of the experimental trials and follow-up analyses is presented in the Materials and Methods. Please see the figures or associated legends for detailed information on sample size and statistical methods.

Preclinical treatment of RT5 mice

To subject RT5 mice to the different treatments, mice from 22 weeks of age displaying blood glucose concentration below 7 mmol/L were screened for the presence of PanNET islet tumors by ultrasound imaging using Vevo2100 and Vevo3100 systems with MS550D 40MHz transducer (Visual Sonic). RT5 mice were randomly assigned to the different treatment groups based on the cumulative tumor burden. The average starting tumor burden was 28 mm² (corresponding to a volume of around 110 mm³), the average starting age was 25 weeks, and the average starting glucose concentration was 5.8 mmol/L for the long-term efficacy studies. Tumors were monitored by ultrasound imaging every two weeks or every four weeks for complete responders for maximal 16 weeks. Blood glucose concentration was monitored weekly using an Accu-Chek glucometer (Roche). The criteria for the endpoint were defined by the tumor burden, hypoglycemia (blood glucose at or below 3 mmol/L), general health status, and loss of body weight (more than 15%). Before processing the organs for chemokine analyses of T cells and macrophages by flow cytometry, mice were treated with 250 µg Brefeldin A for 6 h followed by euthanasia.

Glioma mouse model

For the orthotopic transplantation model involving the GL261 syngeneic model, 100,000 cells were intracranially engrafted as previously described.³⁹ C57BL/6J mice (both males and females) were intracranially injected at 8–11 weeks of age using a stereotactic frame under full anesthesia with a mix of Fentanyl, Midazolam and Medetomidine. The injections were performed using the following coordinates: 2.0mm anterior/posterior, 1.5 mm medial/lateral, and 2.3 mm dorsal/ventral from the bregma. Animals were revived from anesthesia (with a triple-shot mix of Naloxon, Flumazenil and Atipamezol). All animal studies were performed in accordance with the experimental license VD3183 approved by the Veterinary Authorities of the Canton Vaud.

MRI imaging

Tumor growth of GL261 gliomas was monitored with T2-weighted 1H MRI scans on a 3T MRI machine (Bruker). The mice were selected for treatment when the tumors reached approximately 10 mm³ of volume. Before processing the organs for chemokine analyses of T cells and macrophages by flow cytometry, mice were treated with 250 µg Brefeldin A for 6 h followed by euthanasia.

Drugs and dosing regimen

Murine-specific antibody molecules were administered by i.p. injection with the following amounts per mouse: anti-muPD-1-low: 22.75µg, q1wk (anti-PD-1^{low}, equimolar to PD1-IL2v); anti-muPD-1-high: 250 µg, q1wk (anti-PD-1^{high}, therapeutic dose); DP47-muIL2v (IgG-IL2v): 25 µg, q1wk; muPD1-IL2v: 25µg (PD1-IL2v), q1wk; anti-muPD-L1 (anti-PD-L1): first dose 250 µg, followed by 125 µg, twice/wk, for a duration of two weeks (pharmacodynamic studies) or eight weeks (long term efficacy studies). All antibodies contain Fc silencing mutations, PD1-IL2v and anti-PD-1 were mulgG1 with DAPG mutations and DDKK for heterodimerization, PD-L1 was either mulgG1-DAPG or mulgG2-PGLALA. All antibodies were purified and analyzed for monomer content, absence of endotoxins, correct identity, and functionality by Roche Innovation Center Zurich, Switzerland. The anti-mouse CD8 (clone 53–6.72), the anti-mouse CD4 (clone GK1.5) and, the anti-mouse IFN γ (clone XMG1.2) monoclonal antibodies were purchased from BioXcell and intraperitoneally injected twice a week at 250 µg/mouse.

Preparation of single cell suspensions

Single cell suspensions of spleens were generated by mashing the spleen through a 40µm cell strainer. Tumors were harvested and minced using a scalpel and digested for 30 min using collagenase A (0.33 U/mL, Roche), dispase (0.85 U/mL, Roche), DNase I (144 U/mL, Roche) in RPMI medium with intermittent shaking at 37°C. Afterward, tumor single cell suspensions were passed through a 70 µm cell strainer. For the glioma model, following the same digestion protocol, tumor-infiltrating immune cells were isolated by Percoll gradient centrifugation (800xg for 45 min with no brake), collected at the interphase between 40 and 80% Percoll (GE Healthcare), and washed twice with FACS buffer(2%FBS/PBS). To monitor CD4 and CD8 depletion, peripheral blood was collected into EDTA-coated tubes. Red blood cells were lysed with PD PharmLyse buffer (BD Biosciences 555,899) according to the manufacturer's instructions. Cells were further used for Flow Cytometry, cell isolation, or scRNA-seq.

Flow cytometry

Single cell suspension of spleens or tumors were blocked with anti-mouse CD16/32 (BioLegend, cat number 101302) for 15min on ice. Live/dead staining was performed with fixable viability stain kits (780, BD 565388 or Red, BD) for 15min on ice. TAG-specific CD8⁺ T cells were stained with SV40 TAG multimer (APC-MHC-H2Kb-VVYDFLKC, University of Lausanne) for 30 min at room temperature, followed by staining of antibodies against surface antigens for 20 min on ice. Intracellular proteins were stained for 2h or overnight on ice after fixation and permeabilization using the FoxP3 staining kit (Invitrogen, cat number 00-5523-00) according to the manufacturer's instructions. The following antibodies were used: CD4-BV510, CD4 PE-Cy7, (BioLegend, clone RM4-5), CD4-PE (Biolegend, clone GK1.5), CD8-BB515, and CD8-PE-Cy7 (BD Biosciences and Biolegend, clone 53–6.7), CD8-PacO (Invitrogen, clone 5H10), PD-1-PE-Cy7 (BioLegend, clone RMP1-30), CD127-BV650 (BioLegend, clone A7R34), FoxP3-PE (Invitrogen, clone FJK-16s), CD218a-APC (eBioscience, clone B3TUNYA), TCF1-BV421 and TCF1-PE (BD Biosciences, clone S33-966), CD3-FITC, CD3-PerCP-Cy5.5 and CD3-PE-Cy5 (eBioscience, clone 145-2C11), Tim3-PE and Tim3-PE/Dazzle 594 (Biolegend, clone B8.2C12), CD11b-PerCP-Cy5.5, CD11b-Biotin, CD11b-PacB and CD11b-PE-Cy7 (eBioscience, clone M1/70), B220-PerCP-Cy5.5 (eBioscience, clone RA3-6B2), CD45-APC-Cy7, CD45-PacO, CD45-BUV395 and CD45-Biotin (Biolegend, Invitrogen, BD

bioscience, and eBioscience, clone 30-F11), CD44-APC-eF780 (eBioscience, clone IM7), CD62L-FITC (Biolegend, clone MEL-14), TNFa-FITC (eBioscience, clone MP6-XT22), GZMB-PE (eBioscience, clone NGZB), IFNg-APC (Biolegend, clone XMG1.2), Arg1-FITC (eBioscience, clone A1exF5), F4/80-PE (eBioscience, clone BM8), Ly6C-PerCP-Cy5.5 (eBioscience, clone HK1.4), Ly6G-PacB (Biolegend, clone 1A8), CD206(Mrc1)-AF647 (Biolegend, clone C068C2), Il-10-APC-Cy7 (Biolegend, clone JES5-16E3), Ki67 PE-Cy7 (eBioscience, clone SolA15). Fluorophore-conjugated streptavidin were used to detect biotinylated antibodies: SA BV421 (Biolegend, 405,226) and SA PacO (Invitrogen, S32365). Samples were analyzed on a BD LSR Fortessa, Gallios (Beckman Coulter), or CytoFLEX LX (Beckman Coulter), and the data was processed with the FlowJo v10.8.0 software and GraphPad Prism v9.

CD31⁺ and CD11b⁺ cell isolations

Endothelial cells were isolated from the tumor following the CD31 Micro-Bead protocol (Miltenyi Biotec). Myeloid CD11b⁺ cells were isolated from the tumor or the cognate spleen using the positive selection Easysep Mouse CD11b positive selection kit II (Stemcell Technologies) for magnetic isolation according to the manufacturer's instructions. Collectively, monocytes, neutrophils, macrophages, and DCs accounted for more than 90% of the isolated cells. CD11b⁺ cells were further used for gene analyses and co-culture assay. CD31⁺ cells were used for gene analyses.

Cell isolation and co-culture experiments

CD8⁺ T cells isolation was performed on the spleen using the Easysep Mouse CD8⁺ T cell Isolation Kit (Stemcell Technologies) for magnetic isolation according to the manufacturer's instructions. For proliferation assays, CD8⁺ T cells were labeled with CFSE and co-cultured with CD11b⁺ cells in a 1:1 ratio with T CD3/CD28 Dynabeads for T cell expansion and activation. Co-cultured cells were harvested 48–72h later, stained with a live dead dye, and analyzed by flow cytometry to assess their proliferation.

RNA isolation, reverse transcription, and quantitative RT-PCR

RNA from cells and tissues was isolated with the RNeasy Plus Micro Kit (Qiagen). All the procedures were performed according to the manufacturer's instructions. A total of 150–250 ng of RNA was used for cDNA synthesis using the PrimeScript RT Master Mix (RR036A, TaKaRa). qRT-PCR was performed using the Rotor-Gene SYBR Green Master Mix (Qiagen).

Immunohistochemistry

Tumors were embedded in OCT and frozen on dry ice. 10 μm thick methanol-fixed sections were subjected to staining with CD8-FITC (BioLegend, clone 53–6.7), PD-1-PE (eBioscience, RMP1-30), CD31-FITC and CD31-PE (BD Biosciences, clone MEC13.3), PD-L1-PE (Invitrogen, clone MIH5), TAG (in house production), anti-rabbit Alexa Fluor 647 (secondary antibody for TAG, ab150075), F4/80-PE (eBioscience, clone BM8), MHCII-FITC (Biolegend, clone M5/114.15.2), Mrc1-AF647 (Biolegend, clone C068C2), High Endothelial Venule -AF488 (eBioscience, clone MECA-79) and counterstained with DAPI (Roche, 10,236,276,001). Sections were imaged on a Leica DM5500 microscope, an Olympus VS120 slide scanner and a Zeiss Axioscan Z1 slide scanner. Images were processed with Adobe Photoshop, ImageJ, and QuPath software.

Single-cell RNA sequencing

Single-cell experiments were performed using the 10X Chromium platform using the 5' v2 kit (dual index, PN-1000263). TCR V(D)J amplification was performed using 10x Chromium Single Cell mouse TCR amplification kit (PN-1000254). Samples were prepared as described in the preparation of single cell suspensions. The 10X sample processing was performed according to established protocols, aiming at 4000 cells/sample. The libraries were sequenced on an Illumina HiSeq4000 platform, with run conditions as per 10X recommendations, aiming at 50'000 reads/cell.

Mapping was performed with CellRanger (v5.0.1, with default parameters) on the mouse reference refdata-gex-mm10-2020-A to which the SV40 large TAG transgene was added (SV40 large TAG is expressed in beta cells under the rat insulin 1 promoter). A total of 17'105 barcodes and 32'286 features for the tumor samples, and 33'776 barcodes and 32'286 features for the spleen samples were then processed using Seurat (v4.0.4). Briefly, features found in a minimum of 5 cells were kept, cells with at least 200 unique features detected were kept. Cells with less than 7500 unique features detected in tumor samples, or less than 4000 unique features in spleen samples, and less than 10% features mapping to the mitochondrial genome were kept for a final set of 13'797 cells and 19'605 genes for the tumor samples, and 29'012 cells and 17'481 genes for the spleen samples. Samples were independently log normalized and integrated using 2000 most variable features. Unsupervised clustering was performed applying the graph-based clustering approach and Louvain algorithm and Uni-form Mani-fold Approximation and Projection (UMAP) dimensional reduction was performed based on the previously computed neighbor graph using the top 30 PCs.

ProjecTILs (v1.0.0,³¹) was used to predict T cell states among the 7757 CD8⁺ and CD4⁺ T cells identified in tumor samples, using tumor-infiltrating T lymphocytes reference atlas (16,803 high-quality single-cell transcriptomes from 25 samples of B16 melanoma and MC38 colon adenocarcinoma tumors from six different studies). ProjecTILs predicts the effects of cell perturbations and identifies gene programs that are altered by the various treatments.

Differential gene expression was computed within each main population and each T cell sub-population using the pseudo-bulk approach implemented in muscat (v1.4.0), using the method edgeR. Genes expressed in at least 10% of the cells per population per sample were retained. The following comparisons were computed: PD1-IL2v + anti-PD-L1 vs. anti-PD-L1, PD1-IL2v + anti-PD-L1 vs. PD1-IL2v, PD1-IL2v vs. anti-PD-L1, and anti-PD-L1 vs. CTRL. Gene Set Enrichment Analysis (GSEA) was performed on the ranked lists of differentially expressed (DE) genes using the Hallmark gene sets collection with clusterProfiler (v3.18.1).

scTCR-seq analysis

Single-cell TCR-sequencing reads were aligned using 10x Genomics Cell Ranger VDJ 5.0.1,⁷⁰ mapping reads to the Mouse reference dataset (GRCm38/Ensembl/10x). VDJTools⁶⁸ version 1.2.1 was used to generate the Rarefaction plot and immunarch⁶⁹ library (version 0.6.4) in R (version 4.0) to calculate Chao1 diversity index as well as Jaccard overlap plots and correlation plots as well

as all the proportion measures. % of T-cells with TCR sequences, TCR total clones, TCR Richness, Evenness, and Shannon diversity were calculated and plots generated using R (version 4.0).

We used the sequences CASSFDERLFF for the CDR3 beta sequence and CVLLSNTGYQNFYF for the CDR3 alpha sequence of TCR-I as well as CASSRAGGQDTQYF for the CDR3 beta and CAASSRAQGGRALIF for the alpha sequence of TCR-IV to identify two known SV40-TAG-specific CD8⁺ T cell clones.^{34,71} We reported for each clone the generalized Levenshtein distance between the sequence and the TCR-I alpha and beta sequences and TCR-IV alpha and beta sequences. Taking the minimum of the alpha and the beta chain and checking if this minimum is strictly lower than two, we assessed if or not this clone corresponds to TCR-I or TCR-IV.

Mouse VDJDB (vdjdb.cdr3.net/)⁷² was used to annotate the clones that mapped to the database with Levenshtein distance less than two, removing the first and two last amino acids. For the single-cell UMAP plot: Using Seurat, using the FeaturePlot function, each cell was colored by the presence in this dataset of the clonotype.

NicheNet analyses

Potential interactions between selected sets of sender and receiver cell populations were queried through NicheNet (package nicheNet, version 1.0.0).³⁸ The analysis pipeline was performed as outlined by the authors with minor adjustments. Significantly up-regulated genes ($p_{\text{adj.loc}} \leq 0.05$ and $\log_{2}FC \geq 1$) in receiver cell populations in PD1-IL2v vs anti-PD-L1 and PD1-IL2v + anti-PD-L1 vs anti-PD-L1 treatments comparisons were defined as genesets of interest. The lists of putative ligands were filtered by Pearson Correlation Coefficient ($PCC > 0.1$). Furthermore, only ligands expressed in the sender cell populations (i) with an average scaled expression score above 1.5, (ii) in at least 25% of cells, (iii) and significantly up-regulated ($p_{\text{adj.loc}} \leq 0.05$ and $\log_{2}FC \geq 1$) in CTRL vs anti-PD-L1 treatments comparisons were retained. Cognate receptors were selected when expressed in at least 20% of cells in the receiver cell populations.

Data availability

ScRNA-seq data analysis presented in this study are deposited in the Gene Expression Omnibus with the submission number: GSE197854.

QUANTIFICATION AND STATISTICAL ANALYSIS

Quantification of tissue staining

Images were analyzed using the QuPath software (version 0.2.3)⁶⁷

Necrotic and DAPI-negative areas were excluded.

For total CD8⁺ T cells, F4/80⁺, Meca79⁺, CD31⁺, Mrc1⁺ and MHCII⁺ cells.

Using QuPath software, a tumor area was annotated as a region of interest. Positive cell detection (using DAPI) was used with an intensity threshold >100 . Using Fiji-ImageJ software, a Gaussian blur was applied ($\sigma = 2$) to subtract the noise. The binary masks were created by applying a manual threshold for the positive signal (B&W). The Watershed function was utilized to avoid touching objects. The number of cells was obtained by applying the 'analyze particle' function with a >100 pixels surface particle size.

For Meca79⁺ CD31⁺ cells, Mrc1⁺F4/80⁺ TAMs and MHCII⁺F4/80⁺ TAMs.

The binary masks were created as described above. The double-positive cells were determined with the Image Calculator using the 'AND' operator between CD31⁺ (total vasculature) and Meca79⁺ (HEVs); F4/80⁺ and Mrc1⁺ (M2-like TAMs) or MHCII⁺ (pro-inflammatory TAMs) masks and divided by the total CD31⁺ cells or F4/80⁺ cells respectively.

Statistical analysis

GraphPad Prism (version 9.4.1) was used to performed the statistical analyses.

Data in all quantitative panels are presented as mean \pm SEM, unless otherwise stated in the figure legends. Statistical analyses were assessed with unpaired Mann-Whitney test to compare two groups, one-way ANOVA Kruskal-Wallis with Dunn's multiple comparisons test or two-way ANOVA to compare multiple groups, and Log rank Mantel-Cox test for survival analyses as stated in the figure legends; p values are reported in the figures and figure legends. Statistical significance is indicated as * $p < 0.05$, ** $p < 0.01$, *** $p < 0.001$, **** $p < 0.0001$ and ns (non-significant).